The Astrophysical Journal, 786:55 (22pp), 2014 May 1 doi:10.1088/0004-637X/786/1/55

INTERSTELLAR AND EJECTA DUST IN THE CAS A SUPERNOVA REMNANT

Richard G. Arendt[1,2], Eli Dwek[2], Gladys Kober[2,3], Jeonghee Rho[4,5], and Una Hwang[6,7]
[1] CRESST, University of Maryland, Baltimore County, Baltimore, MD 21250, USA; Richard.G.Arendt@nasa.gov
[2] NASA Goddard Space Flight Center, Code 665, Greenbelt, MD 20771, USA
[3] Department of Physics, IACS, Catholic University of America, Washington, DC 20064, USA
[4] SETI Institute, 189 Bernardo Avenue, Mountain View, CA 94043, USA
[5] SOFIA Science Center, NASA Ames Research Center, MS 211-3, Moffett Field, CA 94035, USA
[6] NASA Goddard Space Flight Center, Code 662, Greenbelt, MD 20771, USA
[7] The Henry A. Rowland Department of Physics and Astronomy, Johns Hopkins University, 3400 North Charles Street, Baltimore, MD 21218, USA
Received 2013 October 7; accepted 2014 March 12; published 2014 April 16

ABSTRACT

Infrared continuum observations provide a means of investigating the physical composition of the dust in the ejecta and swept up medium of the Cas A supernova remnant (SNR). Using low-resolution *Spitzer* IRS spectra (5–35 μm), and broad-band *Herschel* PACS imaging (70, 100, and 160 μm), we identify characteristic dust spectra, associated with ejecta layers that underwent distinct nuclear burning histories. The most luminous spectrum exhibits strong emission features at ∼9 and 21 μm and is closely associated with ejecta knots with strong Ar emission lines. The dust features can be reproduced by magnesium silicate grains with relatively low Mg to Si ratios. Another dust spectrum is associated with ejecta having strong Ne emission lines. It has no indication of any silicate features and is best fit by Al_2O_3 dust. A third characteristic dust spectrum shows features that are best matched by magnesium silicates with a relatively high Mg to Si ratio. This dust is primarily associated with the X-ray-emitting shocked ejecta, but it is also evident in regions where shocked interstellar or circumstellar material is expected. However, the identification of dust composition is not unique, and each spectrum includes an additional featureless dust component of unknown composition. Colder dust of indeterminate composition is associated with emission from the interior of the SNR, where the reverse shock has not yet swept up and heated the ejecta. Most of the dust mass in Cas A is associated with this unidentified cold component, which is $\lesssim$0.1 $M_\odot$. The mass of warmer dust is only ∼0.04 $M_\odot$.

Key words: dust, extinction – infrared: ISM – ISM: individual objects: (Cassiopeia A) – ISM: supernova remnants

Online-only material: color figures

1. INTRODUCTION

Interstellar dust models that fit the average interstellar extinction curve, the diffuse infrared emission and scattering, polarization, and abundance constraints employ a very limited variety of dust compositions, consisting primarily of polycyclic aromatic hydrocarbons (PAHs), graphite or amorphous carbon, and astronomical silicates (Li & Draine 2001; Zubko et al. 2004; Brandt & Draine 2012; Siebenmorgen et al. 2014). Yet observations of the primary sources of interstellar medium (ISM) dust (or at least the metals therein), asymptotic giant branch (AGB) stars, and supernovae (SNe), reveal a significantly richer variety of dust compositions. For example, magnesium sulfide (MgS) is inferred from spectral features of pre-planetary nebulae (Omont et al. 1995) with similar features in carbon-rich AGB stars and PNe (Forrest et al. 1981; Hony et al. 2002). Cherchneff (2012) contains a detailed model of the formation of a wide variety of molecules and dust in an AGB star. More directly, presolar grains of SN or stellar origin, such as silicate carbide (SiC), silicon nitride (Si_3N_4), and aluminum-, calcium- and titanium-oxides, are found as meteoritic inclusions (e.g., Zinner 2008). The absence of a wide variety of specific compositions in interstellar dust models indicates that these compositions are not required for fitting various manifestations of dust in the general ISM, either because of their low abundance relative to silicates and carbonaceous dust, or due to the fact that they may have been processed in the ISM.

SNe can be important sources of interstellar dust. They produce all the refractory elements needed for the formation of dust and their ejecta largely retain the compositional inhomogeneity of the progenitor star. They may therefore be sources of dust with unusual chemical and isotopic compositions (Nozawa et al. 2010; Cherchneff & Dwek 2010; Clayton 2013; Biscaro & Cherchneff 2014). Furthermore, SNe are drivers of the chemical evolution in galaxies and are therefore potentially the most important sources of interstellar dust. In young populations, before low-mass stars have evolved off the main sequence, e.g., high-redshift galaxies, SNe are the dominant source of thermally condensed dust, though additional grain growth by cold accretion within dense clouds may be required to explain the inferred dust mass in these systems (Dwek & Cherchneff 2011; Valiante et al. 2011). Determining the mass and composition of SN-condensed dust is therefore key for understanding the origin, evolution, and processing of dust in galaxies.

The Cas A remnant is an ideal object for studying the composition and abundance of dust that formed in the ejecta of a core collapse SN. The SN was not definitively recorded at the time that it occurred. Studies of the expansion of the supernova remnant (SNR) estimate that the explosion occurred in the year 1681 ± 19 (Fesen et al. 2006). Fortunately, light echoes of the Cas A SN have allowed studies of this old event with modern instruments. Such observations have revealed that Cas A was a Type IIb SN (Krause et al. 2008) with distinct asymmetry in its explosion (Rest et al. 2011). Dynamical and compositional asymmetries are still imprinted on the Cas A SNR today, but the dominant structure of the Cas A SNR is characterized by a clear distinction between the forward shock sweeping up the ISM (and/or circumstellar medium, CSM), and the reverse shock through which the SN ejecta is expanding.

The ejecta consists of three main components. The first, containing most of the mass, is a low-density phase that is heated by the reverse shock to X-ray-emitting temperatures

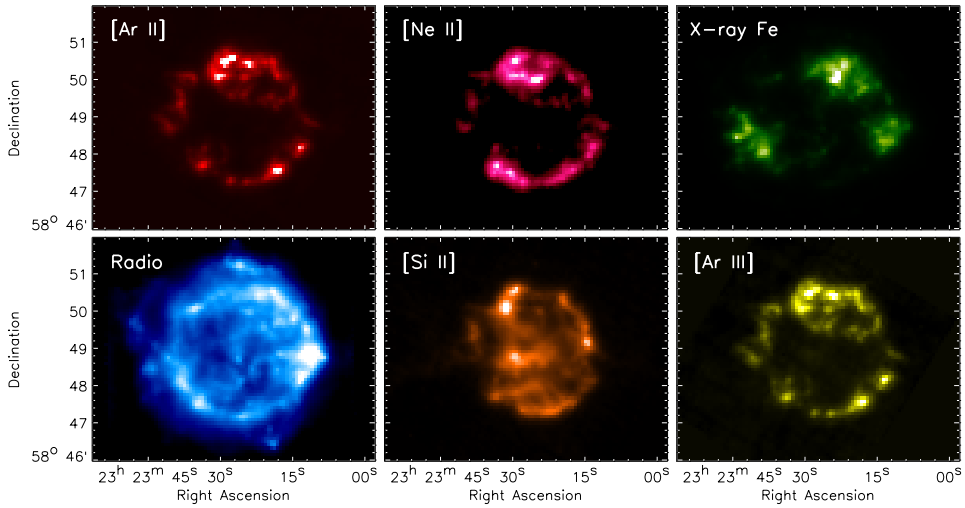

Figure 1. Spatial templates used to signify regions that may contain dust distinguished by different composition, origin (ejecta vs. ISM), and/or heating. The [Ar II] 6.99 μm, [Ne II] 12.81 μm, [Si II] 34.8 μm, and [Ar III] 8.99 μm lines are derived from the IRS data cube. The X-ray Fe emission is from Hwang et al. (2004) and the VLA 6 cm radio map is from DeLaney (2004).

(A color version of this figure is available in the online journal.)

($\gtrsim 10^6$ K). The second component consists of dense fast-moving knots (FMKs) that have gone through the reverse shock, and are radiatively cooling by line emission at optical and infrared (IR) wavelengths. A third component comprises ejecta that has not yet encountered the reverse shock and is primarily heated by the ambient radiation within the SNR interior.

In this paper, we revisit the analysis of the mid- to far-IR spectra of the dust in Cas A. IR emission can arise from dust in each of the ejecta components discussed above, as well as the CSM or ISM that is shocked by the advancing SN blast wave, i.e., the forward shock. Our main goal is to separate and identify different types of dust that are associated with different ejecta (and ISM or CSM) components and to determine the spatial distribution of the different types of dust. Our approach will provide important information on the physical processes that facilitate or inhibit the nucleation of dust in the different layers of the ejecta, the resulting dust composition, and the dust heating mechanisms that give rise to the IR emission. Our approach is different from previous ones (Ennis et al. 2006; Rho et al. 2008) that only grouped the IR emission into distinct spectral components, with no relation to the nature of the ejecta from which they originated.

The outline of our analysis is as follows.

1. We identify a set of *spatial templates* that are used as the initial indicators of regions of different ejecta composition and/or physical conditions around the SNR. These are illustrated in Figure 1 and the details of their derivation are presented in the Appendix.
2. For each spatial template, we identify *zones* (subregions) where that template is most prominent with respect to the other templates. These are described in Section 3.1 and shown in Figure 2.
3. Within each of the zones and at each wavelength, we use the spatial correlation between the data and the template (see Equation (1)) to derive the *characteristic spectra* associated with each spatial template. These are presented in Section 3.1 and Figure 3. Analysis of these characteristic spectra provides indications of the dust composition and temperature(s).
4. Finally, at each spatial location across the entire SNR, the spectrum is decomposed as a linear combination of the characteristic spectra. The coefficients of these decompositions are mapped out to reveal images of the *spatial distributions* of the dust that gives rise to each characteristic spectrum. This is described in Section 3.2 and illustrated in Figure 4.

Section 2 of this paper describes the preparation of the *Spitzer* Infrared Spectrograph (IRS) data to create a spectral cube of the dust continuum emission of Cas A. Section 3 explains the data analysis steps described above, and the details and results of modeling the characteristic spectra are presented in Section 4. In Section 5, we discuss the results, including what conclusions can and cannot be drawn concerning the dust composition and mass. The work is summarized in Section 6.

2. DATA PREPARATION

Our work began with the low-resolution IRS spectral data cubes used by Rho et al. (2008). There are four cubes, generated from the first and second order spectra in short and long wavelength low-resolution modules. At each wavelength, the data were convolved to the spatial resolution at the longest IRS wavelength, 38.33 μm, using kernels derived from Tiny Tim/*Spitzer* (STINYTIM)[8] point-spread functions (PSFs), according to Gordon et al. (2008). The three shorter wavelength cubes were then reprojected to the same scale and orientation as the longest wavelength (SL1) cube. The data are then combined into a single IRS low-resolution cube covering 5–38 μm with a fixed spatial resolution. Weighted averages were used at the wavelengths that overlap between the different spectral orders and modules.

For the purpose of analyzing the dust emission, we created a continuum spectral cube by replacing all emission lines with smooth polynomial fits to the continuum on either side of each line. This procedure is performed independently for each spatial pixel of the cube and each line. It avoids any need to fit the lines themselves, which can be found at various velocity components at each pixel because of the high expansion velocities of Cas A. The lines that were thus removed are listed in the row and column headings of Table 1. Finally, to remove remaining artifacts and

[8] http://irsa.ipac.caltech.edu/data/SPITZER/docs/dataanalysistools/tools/contributed/general/stinytim/

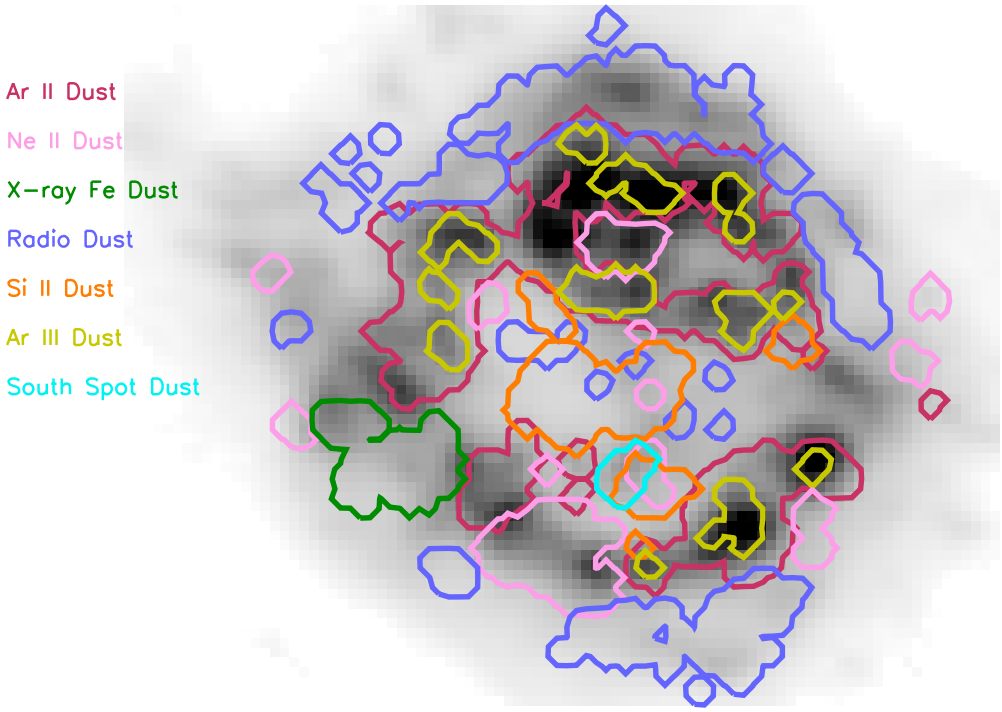

Figure 2. Depiction of the zones within which the characteristic spectra of each spatial template were extracted. These zones correspond to the regions where the templates shown in Figure 1 are dominant (apart from the nearly ubiquitous Ar II). The additional "South Spot" zone was identified as the primary region where there is relatively strong continuum emission that is not traced by any of the spatial templates.

(A color version of this figure is available in the online journal.)

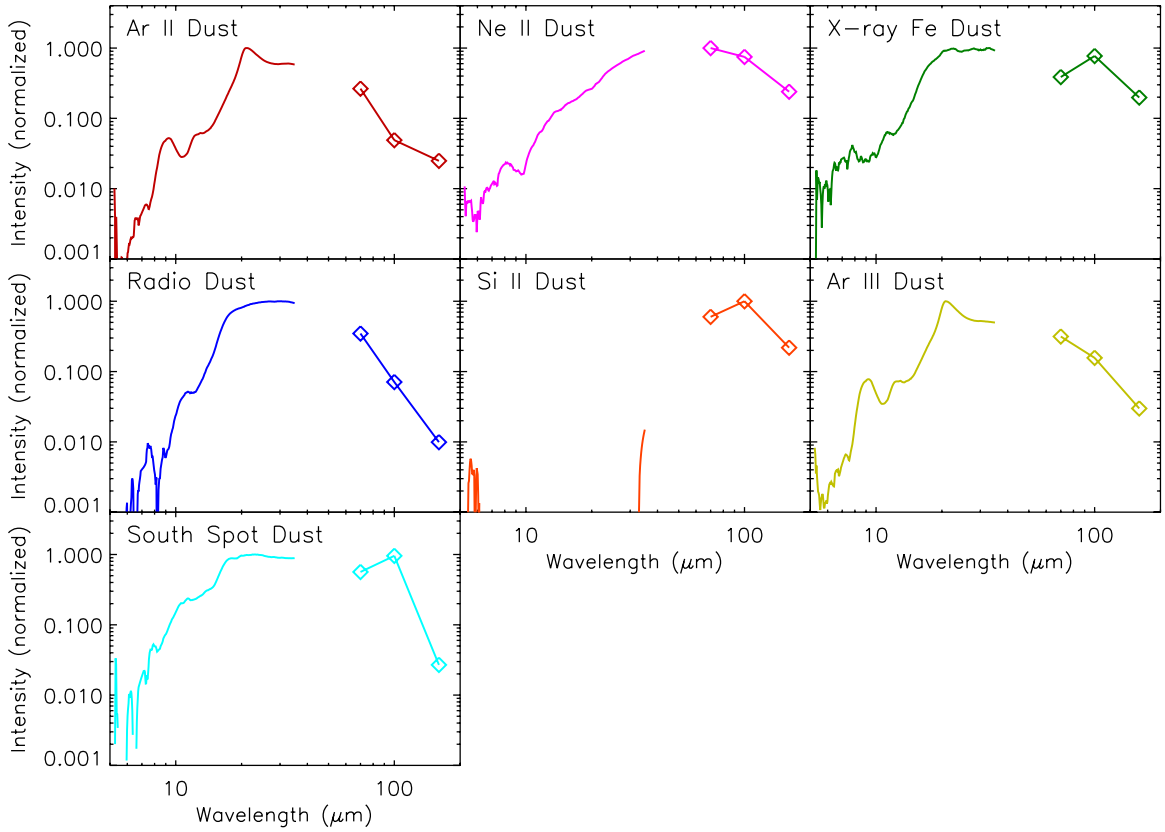

Figure 3. Characteristic spectra extracted for each of the spectral zones defined in Figure 2. In each case, the solid line from 5–35 μm is the IRS data. The three points at 70, 100, and 160 μm are broadband *Herschel* PACS data. (The Si II dust has no significant emission at $\leqslant$35 μm).

(A color version of this figure is available in the online journal.)

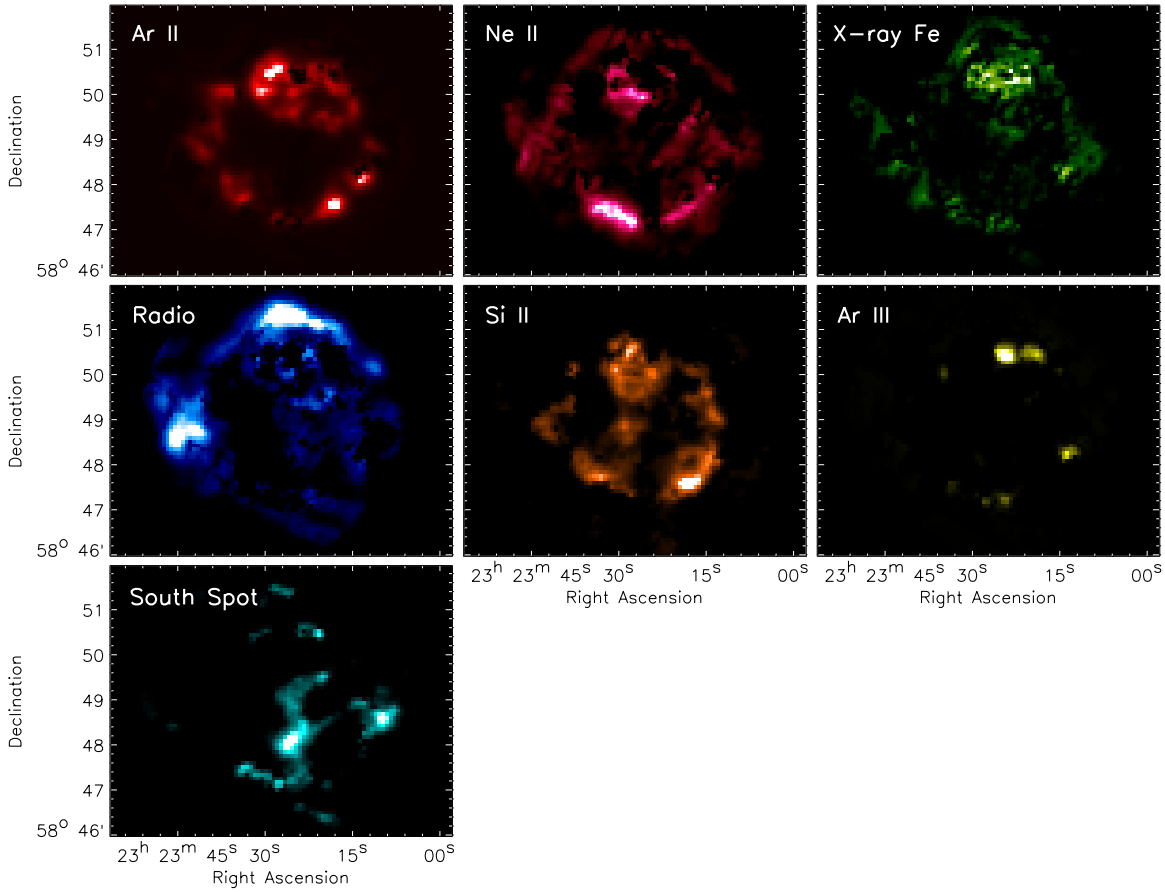

Figure 4. Spatial distribution of the dust associated with each of the characteristic spectra shown in Figure 3.
(A color version of this figure is available in the online journal.)

improve the signal to noise, the continuum cube was smoothed in wavelength to a spectral resolution of $R = \lambda/\Delta\lambda \approx 20$, and trimmed to a maximum wavelength of 35 μm. After this smoothing, there are only ~40 truly independently sampled wavelengths in the data cube.

Longer wavelength information was obtained by using *Herschel* PACS (Pilbratt et al. 2010; Poglitsch et al. 2010) observations at 70, 100, and 160 μm, with the appropriate spatial convolution of the 70 and 100 μm images whose native resolution is better than the IRS at 38 μm. (All *Herschel* data used here were Level 2 products generated from Standard Product Generation SPG 4.1.0.) At 160 μm the SNR is substantially confused by ISM emission. This confusion was reduced by subtracting an empirically scaled version of the *Herschel* SPIRE (Griffin et al. 2010) 250 μm image in which the synchrotron emission of the SNR was subtracted by extrapolation from the 350 and 500 μm bands. The subtraction is an improvement, but is still imperfect, in part due to the lower spatial resolution of the longer wavelength SPIRE data.

The synchrotron emission is removed from the final *Spitzer* continuum cube by subtraction of the Very Large Array (VLA) radio template (DeLaney 2004) extrapolated assuming a power law spectrum $S_\nu \sim \nu^{-0.71}$.

3. ANALYSIS

3.1. Derivation of Characteristic Spectra

One of the primary goals of this analysis was to find the continuum spectra of dust that is found in regions of various physical parameters and compositions throughout the SNR. The regions to be investigated are identified via six distinct spatial templates. These templates are shown in Figure 1 and Table 2, and are described in more detail in the Appendix. To identify the spectra associated with each of the six emission templates, we superimposed all the templates and for each one we identified the zones where its relative emission was the dominant component. Because of the strong and widespread [Ar II] emission, in some cases the zones necessarily included [Ar II] emission as well. The zones selected for each of the templates are outlined in Figure 2.

For all pixels, i, of each zone of the six selected emission templates, $T_j(i)$, the data $D(i, \lambda)$ can be represented by

$$D(i,\lambda) = \sum_{j=1}^{6} S_j(\lambda) T_j(i) + C(\lambda). \quad (1)$$

The parameters $C(\lambda)$, a constant term (which should be small) to account for errors in the background levels, and $S_j(\lambda)$, the spectra associated with each of the templates, can thus be derived via a least-squares fit or linear regression between the data and the templates.

For the Ar II zone, the sum is strongly dominated by this template, and $S_{\rm Ar\,II}(\lambda)$ is determined as the slope of a linear least squares fit between $D(i, \lambda)$ and $T_{\rm Ar\,II}(i)$. Some Ar II emission is unavoidable in all other zones; therefore, for the other zones the spectra $S_j(\lambda)$ were derived using a linear regression between $D(i, \lambda)$ and two templates: $T_j(i)$ and $T_{\rm Ar\,II}(i)$. The characteristic spectra derived are shown in Figure 3.

Table 1
Linear Correlation Coefficients between the Spatial Templates

	[Ar II]	**[Ar III]**	[S IV]	[Ne V]	[Fe II]	[S III]	IRAC 8 μm	**[Ne II]**	[Ne III]	IRAC 4.5 μm	[O IV]	[S III]	**[Si II]**	**X-ray Fe**	X-ray Si	**Radio**
[Ar II] 6.99 μm	1.00	0.99	0.97	0.89	0.77	0.97	0.97	0.76	0.76	0.88	0.83	0.84	0.54	0.44	0.67	0.54
[Ar III] 8.99 μm	...	1.00	0.97	0.88	0.78	0.95	0.97	0.73	0.73	0.87	0.82	0.83	0.56	0.46	0.68	0.54
[S IV] 10.51 μm	...	...	1.00	0.85	0.74	0.96	0.93	0.74	0.75	0.84	0.88	0.89	0.66	0.41	0.65	0.55
[Ne V] 14.32 μm	...	...	...	1.00	0.73	0.90	0.85	0.78	0.81	0.84	0.82	0.82	0.56	0.45	0.65	0.53
[Fe II] 17.94 μm	...	...	...	...	1.00	0.74	0.76	0.58	0.61	0.73	0.67	0.65	0.45	0.34	0.48	0.45
[S III] 18.71 μm	...	...	...	...	...	1.00	0.92	0.77	0.79	0.85	0.88	0.90	0.64	0.46	0.70	0.58
IRAC 8 μm	...	...	...	...	...	...	1.00	0.70	0.70	0.87	0.75	0.76	0.45	0.43	0.63	0.47
[Ne II] 12.81 μm	...	...	...	...	...	...	...	1.00	0.96	0.90	0.81	0.73	0.50	0.37	0.50	0.48
[Ne III] 15.56 μm	...	...	...	...	...	...	...	...	1.00	0.88	0.83	0.75	0.54	0.42	0.52	0.50
IRAC 4.5 μm	...	...	...	...	...	...	...	...	...	1.00	0.81	0.76	0.49	0.45	0.58	0.54
[O IV] 25.89 μm	...	...	...	...	...	...	...	...	...	...	1.00	0.93	0.83	0.39	0.64	0.62
[S III] 33.48 μm	...	...	...	...	...	...	...	...	...	...	...	1.00	0.84	0.41	0.62	0.62
[Si II] 34.82 μm	...	...	...	...	...	...	...	...	...	...	...	...	1.00	0.23	0.42	0.55
X-ray Fe	...	...	...	...	...	...	...	...	...	...	...	...	...	1.00	0.71	0.65
X-ray Si	...	...	...	...	...	...	...	...	...	...	...	...	...	...	1.00	0.75
Radio	...	...	...	...	...	...	...	...	...	...	...	...	...	...	...	1.00

Note. Spatial templates in boldface were selected as the basis for further analysis.

Table 2
Chosen Spatial Templates

Template	Purpose
[Ar II]	Trace dust in the most dominant line-emitting ejecta
[Ne II]	Trace dust in a distinctly different ejecta component from higher layers of the SN
X-ray Fe	Trace dust in hotter, low-density ejecta from the inner portion of the SN
Radio	Trace ISM or CSM dust swept up behind the forward shock
[Si II]	Trace dust in slow-moving ejecta, yet to cross the reverse shock
[Ar III]	Test if dust properties differ in regions where ionization state of the gas is higher

When these derived spectra are multiplied by the spatial templates over the entire SNR (not just within the selected zones) and the result is subtracted from the data cube, we found that there was one region of residual emission that was particularly strong and consistently positive at all wavelengths. This region is in the south central portion of the SNR. One additional zone was created to cover this region (the "South Spot" in Figure 2), and the measured spectrum within this zone is included in Figure 3.

The characteristic spectra are key data that allow for the detailed examination of the nature of the dust in different regions of the SNR. The modeling and analysis of the characteristic spectra are presented in Section 4.

3.2. Spatial Distributions of the Characteristic Spectra

In principle, the spatial templates, $T_j(i)$, and their characteristic spectra, $S_j(\lambda)$, provide a complete description of the continuum data cube. However, because the characteristic spectra were derived only from limited zones of the SNR, it is informative to revisit the data modeling given by Equation (1), but instead using the seven $S_j(\lambda)$ characteristic spectra as known quantities and solve for the spatial distributions, $I_j(i)$, of each spectum over the entire SNR:

$$D(i, \lambda) = \sum_{j=1}^{7} S_j(\lambda) I_j(i) \; + \; C(i). \qquad (2)$$

In this fitting, a constant term, $C(i)$, is still present to account for background errors, but now this constant is a function of position rather than wavelength. If the characteristic spectra are uniquely and perfectly correlated with the spatial templates, then we should find that the spatial distributions are identical to the templates, $I_j(i) = T_j(i)$. Differences between the initial templates and these derived spatial distributions would identify (1) regions where the template emission is present but not accompanied by the characteristic spectrum, and (2) regions where emission matching a characteristic spectrum is present but without corresponding emission of the initial template.

The derived spatial distributions of the different characteristic spectra are shown in Figure 4. Comparison with Figure 1 shows that the derived spatial distribution of the dust associated with Ar II emission is very similar to the input template, $I_{\rm Ar\,II}(i) \approx T_{\rm Ar\,II}(i)$. Differences are more evident for dust associated with Ne II and X-ray Fe emission. However, in both cases, the brightest portions of the derived spatial distributions do follow the original templates, even in areas that were outside of the zones where the characteristic spectra were derived. The spatial distribution of the radio dust (i.e., dust associated with the radio template) is very different from original template, as it tends to be concentrated in areas at the periphery of the SNR that are expected to lie between the forward shock and the reverse shock. Material here should be dominated by swept up interstellar or circumstellar material. Interestingly, the spatial distribution identifies a large area on the east side of the SNR which matches the characteristic spectrum, but had not been within the zone used to define that spectrum. The agreement between the Si II dust's spatial distribution and the initial template is very rough. This spatial distribution is dominated by the morphology of the

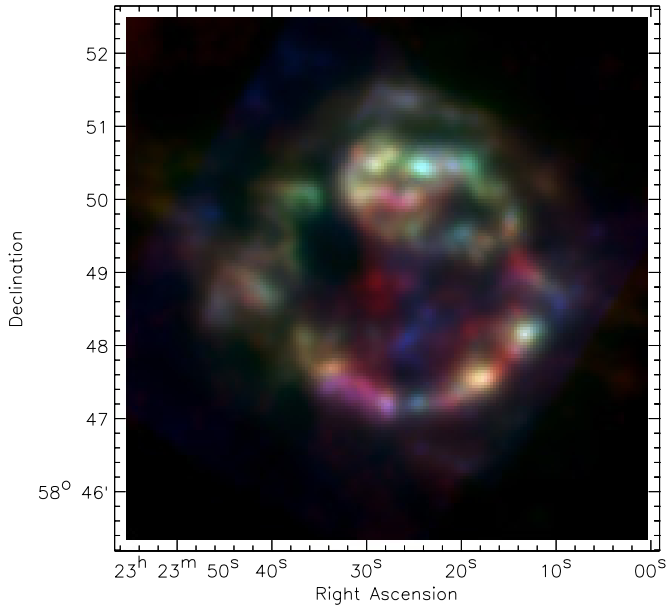

Figure 5. Color image of Cas A dust displays continuum emission at 11.8, 20.8, 70 μm in the blue, green, and red channels, respectively. Comparison with Figure 4 shows that these wavelengths provide good illustration of the different dust types: Ar II = green, Ne II = pink, radio = gray, Si II = red, Ar III = pale cyan, South Spot = purple. (X-ray Fe dust is not clearly distinguished.)

(A color version of this figure is available in the online journal.)

emission at wavelengths $\lambda \geqslant 70\,\mu$m. The spatial distribution of dust matching the Ar III characteristic spectrum is confined to a few of the brightest peaks in the continuum and [Ar III] images.

Guided by these results, we find that a traditional three-color image can be constructed to emphasize the different components via the tint of the continuum emission, as shown in Figure 5. This image combines the emission at 11.8, 20.8, and 70 μm from the smoothed continuum data cube. These wavelengths are chosen by selecting those where the characteristic spectra (Figure 3) have the greatest differences from one another.

3.3. Total Emission

Figure 6 shows the seven Cas A characteristic spectra with their actual intensities (i.e., without normalization). The total emission of each is calculated by integrating the characteristic spectra, $S_j(\lambda)$ (Figure 3), over the regions of the corresponding spatial distributions, $I_j(i)$ (Figure 4). This comparison shows that in the ejecta, the Ar II dust component is dominant at wavelengths from 8 to 35 μm. The dust associated with the radio emission is assumed to be swept up ISM dust rather than ejecta because its spatial distribution turns out to be largely confined to the periphery of the SNR. The brightness of the ISM dust is generally <one third of the brightness of the ejecta dust. The sum of the all the spectra is also shown as a "fit" to the total Cas A spectrum as measured directly from *Spitzer* and *Herschel* data. The general agreement at 10–35 μm indicates that there are no major missing components. At shorter wavelengths, as the SNR emission drops toward the level of the background and the noise, the comparison is not as good.

4. DUST COMPOSITIONS FROM THE CHARACTERISTIC SPECTRA

Six of the seven characteristic spectra (Figure 3) show strong emission at wavelengths from 10 to 40 μm. The *Spitzer* IRS spectra across these wavelengths reveal distinctive features in some of these spectra. The features are suggestive of silicates with peaks of varying sharpness at ~10 and ~20 μm. In order to identify the particular type of silicates and/or other grain compositions that produce each of the characteristic spectra, we assembled a set of grain absorption efficiencies from published optical constants (Table 3), and fitted each characteristic spectrum, $S_j(\lambda)$, as the weighted, $M_{n,i,j}$, sum of different grain mass absorption coefficients, $\kappa_n(\lambda)$, applied to blackbody emission at different temperatures, $B(T_i)$:

$$S_j(\lambda) = \sum_n \sum_{T_i=20\,\mathrm{K}}^{2000\,\mathrm{K}} M_{n,i,j}\kappa_n(\lambda)B(T_i), \quad (3)$$

where n and i are indices for dust composition and temperature, respectively. The mass absorption coefficients, $\kappa_n(\lambda) \equiv 3Q_n(\lambda, a)/4\rho_n a$, or, more directly, the absorption efficiencies, $Q(\lambda, a)$, are calculated using Mie theory and assuming a relatively small grain size $a = 0.01\,\mu$m (e.g., Nozawa et al. 2008, 2010), although $Q(\lambda, a)/a$ is essentially independent of a for $a \lesssim 0.1\,\mu$m at these wavelengths. (ρ_n is the mass density of grains of composition n.)

The MPFIT code (Markwardt 2009) was used to determine coefficients $M_{n,i,j}$ needed to fit each normalized spectrum with

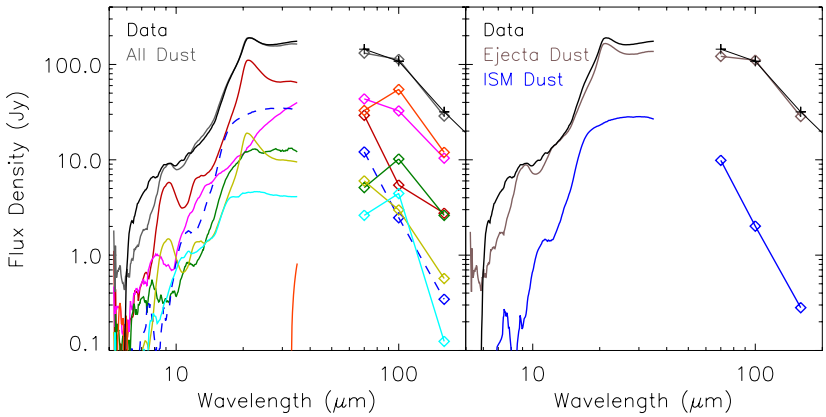

Figure 6. Left: comparison of the relative intensities of each of the spectral types with the total emission of Cas A. The gray line is the sum of all the characteristic spectra. The black line at $\lambda \leqslant 35\,\mu$m is the total of our *Spitzer* IRS spectral cube. The black points at $\lambda \geqslant 70\,\mu$m are the *Herschel* PACS measurements with synchrotron emission and ISM background subtracted (Barlow et al. 2010). Right: comparison of the total Cas A emission with the sum of all the ejecta dust components and the ISM dust component. The ISM dust component is that associated with the radio emission of the forward shock.

(A color version of this figure is available in the online journal.)

Table 3
Dust Compositions Considered for Fitting Spectra

n	Composition	λ Range (μm)	Note	Reference
Silicates				
0	Silicate	0.01–9400		Draine & Lee (1984)
1	$Mg_{0.7}SiO_{2.7}$	0.2–470		Jäger et al. (2003)
2	$MgSiO_3$	0.2–10000		Jäger et al. (2003)
3	$MgSiO_3$	0.1–100000		Dorschner et al. (1995); T. Kozasa (2006, private communication)
4	$MgSiO_3$	0.2–500	Glassy	Jaeger et al. (1994); Dorschner et al. (1995)
5	$Mg_{1.5}SiO_{3.5}$	0.2–6000		Jäger et al. (2003)
6	Mg_2SiO_4	0.2–950		Jäger et al. (2003)
7	Mg_2SiO_4	0.1–100000		Jäger et al. (2003); T. Kozasa (2006, private communication)
8	$MgFeSiO_4$	0.2–500	Glassy	Jaeger et al. (1994); Dorschner et al. (1995)
9	$Mg_{2.4}SiO_{4.4}$	0.2–8200		Jäger et al. (2003)
Protosilicates				
10	Ca Protosilicate	7.6–25	A—unheated	Dorschner et al. (1980)
11	Ca Protosilicate	7.7–25	B—450C	Dorschner et al. (1980)
12	Ca Protosilicate	7.8–25	C—695C	Dorschner et al. (1980)
13	Fe Protosilicate	8.2–40	D—unheated	Dorschner et al. (1980)
14	Fe Protosilicate	8–40	E—490C	Dorschner et al. (1980)
15	Mg Protosilicate	8–40	F—485C	Dorschner et al. (1980)
Silica				
16	SiO_2	0.1–500	Am	Philipp (1985); T. Kozasa (2006, private communication)
17	SiO_2	5–500		Philipp (1985)
18	SiO_x	5.6–520	Extrap. at $\lambda > 65\,\mu$m	Rinehart et al. (2011)
SiC, Si				
19	α SiC	0.1–1000	21 μm : $Q_{abs}/a = 0$	Jiang et al. (2005)
20	α SiC	0.1–1000	21 μm : $Q_{abs}/a = 100$	Jiang et al. (2005)
21	α SiC	0.1–1000	21 μm : $Q_{abs}/a = 10^3$	Jiang et al. (2005)
22	α SiC	0.1–1000	21 μm : $Q_{abs}/a = 10^4$	Jiang et al. (2005)
23	β SiC	0.1–1000	21 μm : $Q_{abs}/a = 0$	Jiang et al. (2005)
24	β SiC	0.1–1000	21 μm : $Q_{abs}/a = 100$	Jiang et al. (2005)
25	β SiC	0.1–1000	21 μm : $Q_{abs}/a = 10^3$	Jiang et al. (2005)
26	β SiC	0.1–1000	21 μm : $Q_{abs}/a = 10^4$	Jiang et al. (2005)
27	Si	0.02–247.7	am	Piller (1985); T. Kozasa (2006, private communication)
28	Si	0.07–433.3	cr	Edwards (1985); T. Kozasa (2006, private communication)
C, Fe				
29	Meteoritic Diamond	0.02–110		Braatz et al. (2000); Mutschke et al. (2004)
30	PAH	0.01–9400		Draine & Li (2007)
31	PAH^+	0.01–9400		Draine & Li (2007)
32	Graphite	0.01–9400		Draine & Lee (1984)
33	Carbon	0.01–9400	Amorphous "ac"	Rouleau & Martin (1991)
34	Carbon	0.01–9400	Amorphous "be"	Rouleau & Martin (1991)
35	Carbon	0.1–3000	Glass	Edoh (1983); T. Kozasa (2006, private communication)
36	Fe	0.1–100000		Lynch & Hunter (1991); T. Kozasa (2006, private communication)
Al Oxides				
37	Al_2O_3	7.8–500	Porous	Begemann et al. (1997)
38	Al_2O_3	7.8–200	Compact	Begemann et al. (1997)
Oxides				
39	$MgAl_2O_4$	2–10000	Natural	Fabian et al. (2001)
40	$MgAl_2O_4$	2–6800	Natural, annealed	Fabian et al. (2001)
41	$Mg_{1.01}Al_{1.99}O_4$	1.67–6825	Nonstoich. spinel	Zeidler et al. (2011)
42	$Mg_{0.94}Al_{2.04}O_4$	1.67–6825	Nonstoich. spinel	Zeidler et al. (2011)
43	$Mg_{0.82}Al_{2.12}O_4$	1.67–6825	Nonstoich. spinel	Zeidler et al. (2011)
44	$Mg_{0.73}Al_{2.17}O_4$	1.67–6825	Nonstoich. spinel	Zeidler et al. (2011)
45	$Mg_{0.53}Al_{2.31}O_4$	1.67–6825	Nonstoich. spinel	Zeidler et al. (2011)
46	$Mg_{0.43}Al_{2.38}O_4$	2–10000	Nonstoich. spinel	Zeidler et al. (2011)
47	$CaAl_{12}O_{19}$	2–10000	Hibonite	Mutschke et al. (2002)
48	TiO_2 (1)	2–5843	Anatase	Posch et al. (2003); Zeidler et al. (2011)
49	TiO_2 (2)	2–5843	Brookite	Posch et al. (2003); Zeidler et al. (2011)
50	TiO_2 (3)	0.47–36	Rutile	Posch et al. (2003); Zeidler et al. (2011)
51	$CaTiO_4$	2–5820	Perovskite	Posch et al. (2003); Zeidler et al. (2011)
52	$Mg_{0.6}Fe_{0.4}O$	0.2–500		Henning et al. (1995)

Table 3
(Continued)

n	Composition	λ Range (μm)	Note	Reference
53	$Mg_{0.1}Fe_{0.9}O$	0.2–500		Henning et al. (1995)
54	FeO	0.2–500		Henning et al. (1995)
55	Fe_3O_4	0.1–100000		Mukai (1989); T. Kozasa (2006, private communication)
Sulfides				
56	$Mg_{0.9}Fe_{0.1}S$	10–500		Begemann et al. (1994)
57	$Mg_{0.1}Fe_{0.9}S$	10–500		Begemann et al. (1994)
58	FeS	0.1–100000		Semenov et al. (2003); T. Kozasa (2006, private communication)
59	SiS_2	13–60		Begemann et al. (1996)

the constraint that $M_{n,i,j} \geqslant 0$. In the fitting, the dust temperature is constrained to lie on a grid of values ranging logarithmically from $T_i = 20$ to $T_i = 2000$ with $\Delta \log_{10}(T_i) = 0.05$ ($0 \leqslant i \leqslant 40$). Only components with intensities exceeding 10^{-4} times the peak of the fitted spectrum are kept in the final result. For the purpose of fitting, the uncertainties of the characteristic spectra (normalized to a peak of 1.0) were taken to be $\sigma_S = 0.2S$ with a floor of $\sigma_S \geqslant 0.01$. The 20% fractional uncertainty is chosen to represent both the noise in the measurement and systematic errors associated with the data reduction (e.g., joining spectral orders, subtracting spectral lines). The 1% (of peak flux) floor on the uncertainties represents the random noise terms, which generally dominate the spectra at $\lambda \lesssim 10\,\mu$m. These uncertainties are indicated as the gray bands in Figures 14–20. Given these uncertainties, spectral features at ~8–10, 12, and ~18–20 μm reflect real features of the dust spectra, but smaller spectral details and details at shorter wavelengths carry little weight in the fitting.

For each spectrum, an initial set of fits was performed using only one dust composition, n, at a time. No single composition provided a good fit to the spectrum. The fits were repeated using all possible combinations of pairs of compositions (i.e., the left summation in Equation (3) includes only two of the possible values of n). Some combinations explored in this way result in substantial improvements in the fits. Usually the improved fits involved the pairing of a dust composition with strong spectral features with another composition that is relatively "featureless." To determine whether a second "strong-featured" dust component was warranted, we also performed a set of fits using three compositions, but with the constraint that one was required to have a "featureless" emission spectrum. Since all the featureless compositions produce similar results, we fixed either graphite or the "ac" amorphous carbon composition as the required featureless component in these tests.

The quality of the one- and two-composition fits as measured by χ^2 is shown in Figures 7–12. The left panel of each figure shows a matrix of the χ^2 values, with generalized axes corresponding to different compositions. This is useful to get an overview of which pairs of compositions provide the best fits. The general groupings are based on chemical and/or spectral similarity. The right panel of each of the figures displays the same χ^2 values but now plotted as a function of the second composition and color coded according to the first composition. This plot quantifies χ^2 and allows specific compositions to be identified. The results for single-composition fits correspond to the upper envelope of the curves in these plots (or the diagonal of the matrix in the left panels). Examples of the best fitting two- and three-composition models, as well as contrasting models that also provide reasonably good fits, are shown in Figures 14–20. The results for the seven different characteristic spectra are discussed in more detail below.

4.1. Ar II Dust

The characteristic dust spectrum associated with Ar II exhibits the sharpest peaks at 9 and 21 μm and has a third, weaker peak at ~12 μm. The astronomical silicate of the typical ISM does not have silicate peaks sharp enough to produce the observed features. Magnesium silicates (particularly $Mg_{0.7}SiO_{2.7}$, characterized by Mg/Si = 0.7) have peaks that are in roughly the right locations, but their shapes are not a good match to the data. However, when two-composition fits are performed, the addition of a second component lacking strong spectral features (e.g., graphite, amorphous C, or Al_2O_3), can soften and smooth the appearance of the silicate peaks to provide a much better fit to the spectrum.

The best two-component fit (see Figure 14) employs $Mg_{0.7}SiO_{2.7}$ to fit the 9 and 21 μm silicate peaks, and graphite as the featureless component that weakens the relative strength of the peaks. The fit to these peaks is very good, although the weaker 12 μm peak is not fit at all. Despite the overall good fit, the temperature components needed for the Mg silicate are somewhat suspicious. Components at 71–63 K are needed to fit the 21 μm feature, but are too cold to contribute to the 9 μm feature. Conversely, a 500 K component produces the 9 μm peak while contributing little to the 21 μm peak. Small, stochastically heated grains might be expected to be heated to this range of temperatures, but it is problematic that there is no indication of grains at intermediate temperatures (70 K $< T <$ 400 K). This suggests that the absorption efficiencies used here are not a true physical representation of the Ar II dust. The actual dust must either have a relatively stronger 9 μm peak so that it can produce the observed spectrum from cooler dust, or it must have a somewhat lower absorption efficiency at roughly 10–20 μm so that the presence of grains at intermediate temperatures would be required.

As suggested by the best two-component fits, the best three-component fit combines the $Mg_{0.7}SiO_{2.7}$ with graphite (to weaken the silicate peaks) and adds a nonstoichiometric spinel to provide the 12 μm peak (see Figure 14). However, there is still a tendency in this fit to use distinctly different temperatures and/or compositions to fit each different spectral feature. The spinel material that produces the 12 μm peak is required to be at extremely high temperatures so that it only contributes to this peak. Alternate sources of the 12 μm feature are SiO_2 and SiC. For both of these materials, the spectral features are too sharp and slightly too blue to provide a good match when the mass absorption coefficients, $\kappa(\lambda)$, are calculated from Mie theory for spherical grains. However, calculations assuming a continuous

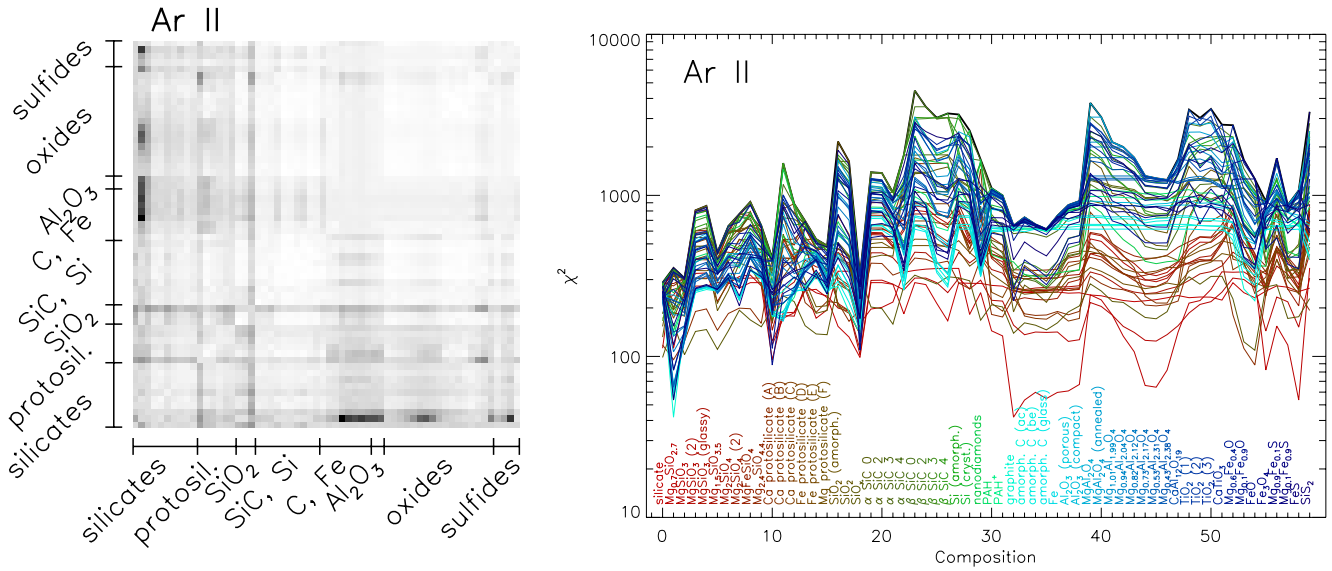

Figure 7. Left: map of χ^2 for two-composition models of the Ar II dust spectrum. Darker shading indicates lower values. The map shows that the lowest values of χ^2 are achieved when one of the silicates (second row from bottom) is paired with the relatively featureless dust such as C, Fe, or Al_2O_3. Good fits are also obtained by pairing this silicate with nonstoichiometric spinels ($MgAl_2O_4$, i.e., oxides) with low Mg/Al ratios. Right: in this alternate depiction of χ^2 for two-composition models, each line plotted shows χ^2 for a given "primary" dust component (as coded by line/label colors) when paired with each possible "secondary" component (as listed in order along the abscissa). Thus, each plotted line corresponds to a row in the matrix shown to the left. Here one can see more specifically that $40 < \chi^2 < 80$ for $Mg_{0.7}SiO_{2.7}$ when paired with the relatively featureless graphite, amorphous C, Fe, Al_2O_3, Fe_3O_4, and FeS, or with the nonstoichiometric spinels with low Mg/Al ratios.

(A color version of this figure is available in the online journal.)

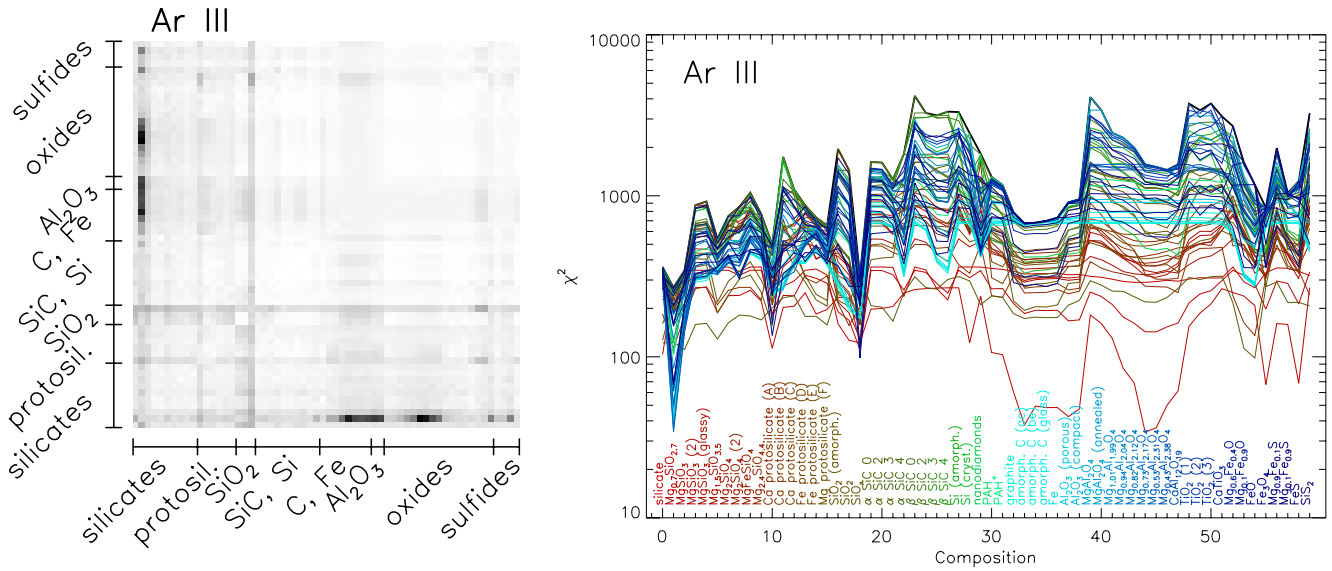

Figure 8. χ^2 as in Figure 7, but for the Ar III dust spectrum. Because the Ar III dust spectrum is very similar to the Ar II dust spectrum, χ^2 for each pair of compositions is very similar in both cases.

(A color version of this figure is available in the online journal.)

distribution of ellipsoids (CDE) for particle shapes (Bohren & Huffman 1983), result in spectral features that are broader and redder. The dust temperatures required to produce the features are also much more reasonable. Figure 14 also shows the fits when CDE calculations are used for a third composition of SiO_2 or α-SiC. SiO_2 provides some contribution to all three of the observed peaks. SiC only provides the 12 μm peak.

4.2. Ar III Dust

The Ar III dust spectrum is very similar to that of the Ar II dust. It was derived separately to determine whether there might be an identifiable shift in dust temperature or composition in these closely related regions. Not surprisingly, the combinations that produced good fits to the Ar II spectrum also produce good fits to the Ar III spectrum (see Figure 15). The increased strength of the 9 μm peak relative to the 21 μm peak would usually suggest warmer dust temperatures in association with the Ar III. However, because the dust features arise largely from separate components of the models, the temperature of the components are largely unchanged, but the relative mass in the hotter components is higher for the Ar III than for the Ar II spectrum.

For the Ar III spectrum, we consistently find that the amorphous C (ac) provides a slightly better fit than the graphite that

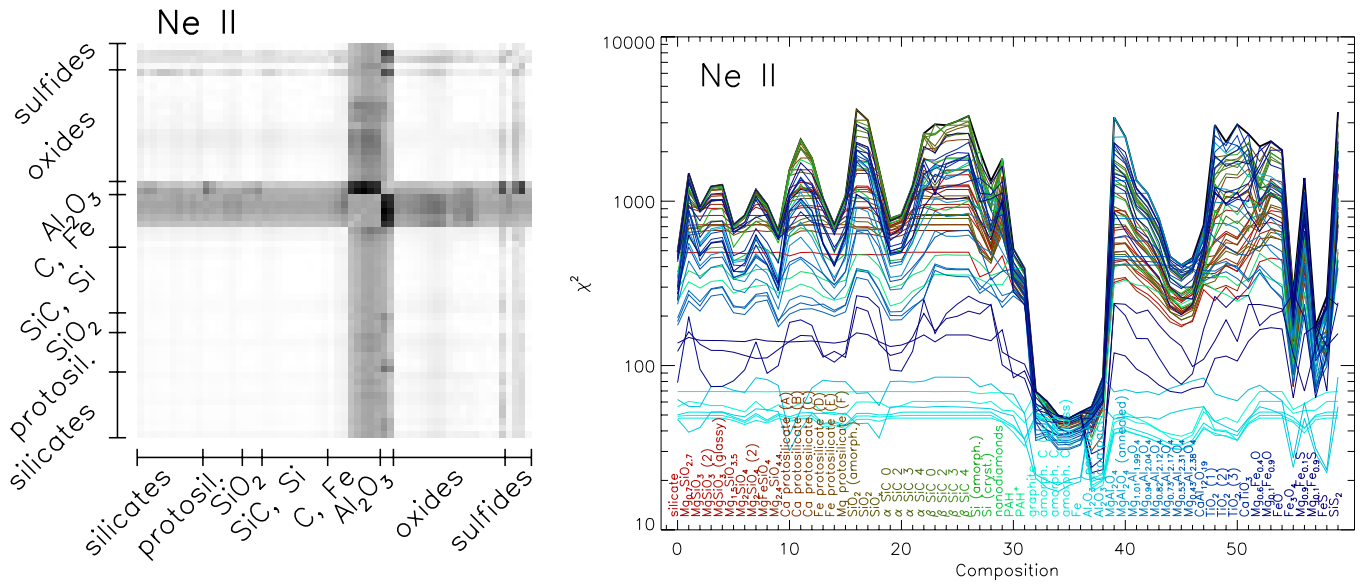

Figure 9. χ^2 as in Figure 7, but for the Ne II dust spectrum. The best models contain either porous or compact Al_2O_3 paired with any of the more featureless dust components.

(A color version of this figure is available in the online journal.)

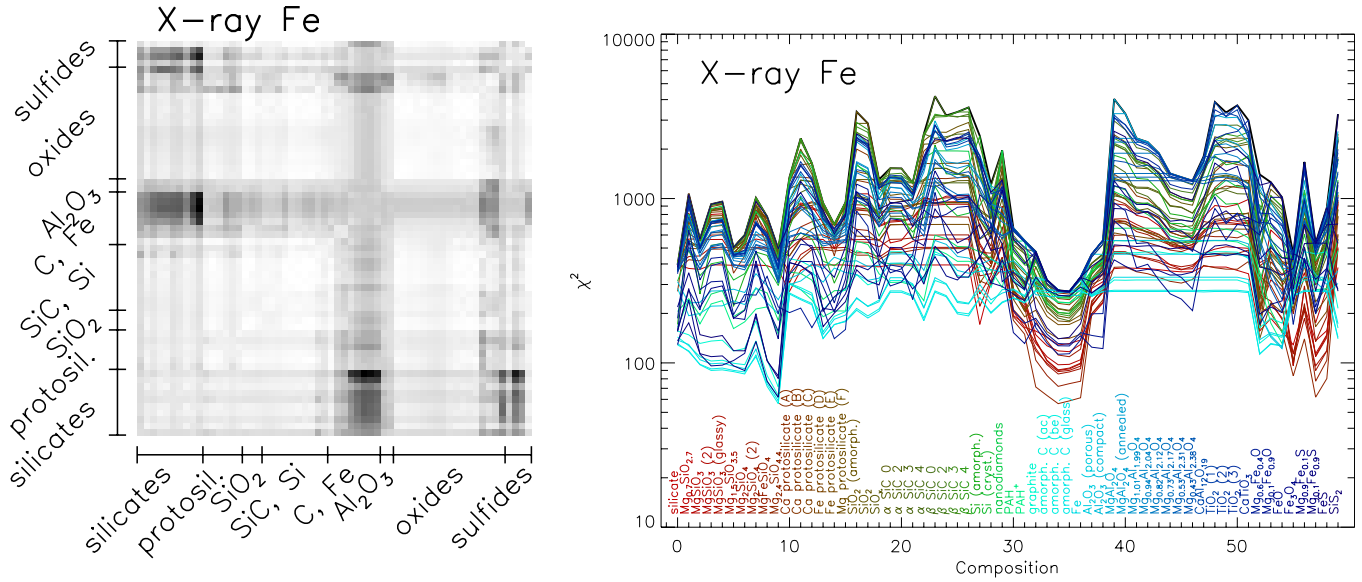

Figure 10. χ^2 as in Figure 7, but for the X-ray Fe dust spectrum. This spectrum is best fit by silicates with high Mg/Si ratios and paired with the relatively featureless compositions.

(A color version of this figure is available in the online journal.)

was somewhat preferred for Ar II spectrum. The Ar III spectrum is also slightly better fit when hibonite ($CaAl_{12}O_{19}$) rather than a spinel composition is used as a third component; however, if CDE calculations are applied, SiO_2 and SiC can again provide equally good fits as the third component.

4.3. Ne II Dust

The dust associated with Ne II exhibits an unusually smooth spectrum. This spectrum excludes significant amounts of warm silicates, but can be fit by compositions with relatively featureless spectra, e.g., graphite and amorphous carbon. The best fits are found by combining featureless dust with Al_2O_3. The latter component has a very broad emission peak between 10 and 20 μm that improves the fit. Figure 16 shows the fit for an amorphous carbon (be) and Al_2O_3 mixture. The fit suggests that some fraction of the Al_2O_3 component is fairly warm ($T \approx 150$ K), while the brightest carbon dust has a temperature of ~75 K. A significant cool (~40 K) dust component helps to fit the *Herschel* data at 70–160 μm. The model attributes this to Al_2O_3, but this identification is degenerate because neither of these compositions have any characteristic spectral features at these wavelengths. The composition of very cool components cannot be very conclusively identified because the shape of the spectra are not very affected by composition.

Figure 16 also shows the best-fit model that does not contain Al_2O_3. In this case, a nonstoichiometric spinel provides a relatively small perturbation to an otherwise smooth amorphous C spectrum. Amorphous C picks up the intermediate temperature (~135 K) components that account for the bulk of the 10–20 μm emission.

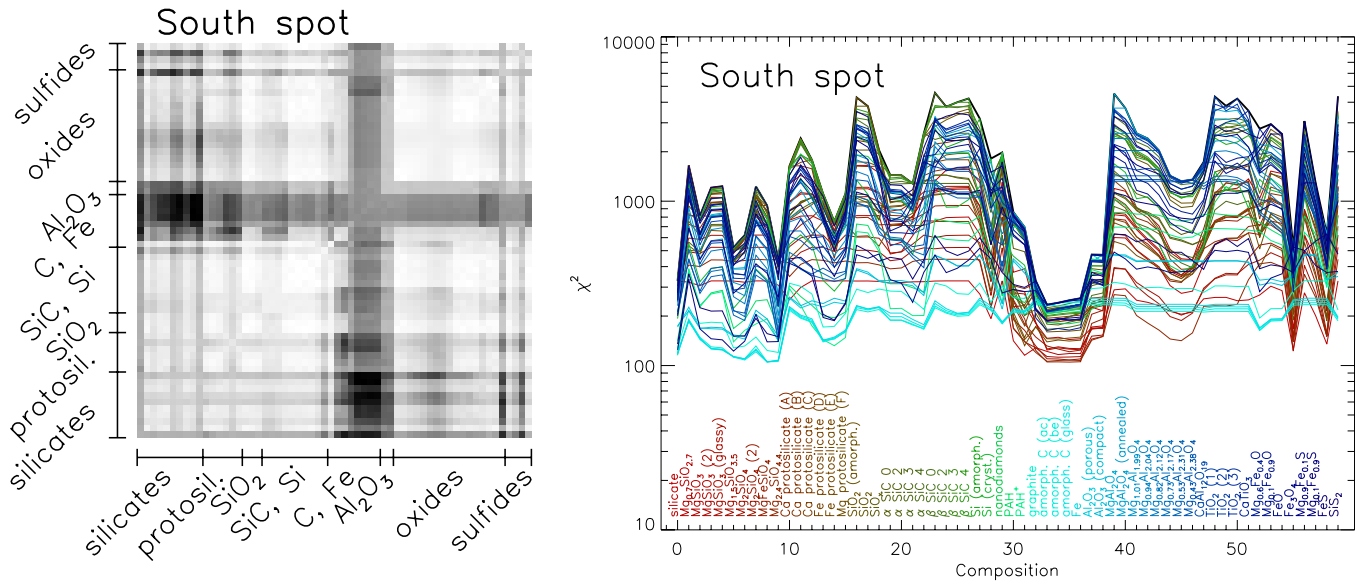

Figure 11. χ^2 as in Figure 7, but for the South Spot dust spectrum. The results here are very similar to those for the X-ray Fe spectrum, but with somewhat less contrast between the best fits and the more marginal ones.
(A color version of this figure is available in the online journal.)

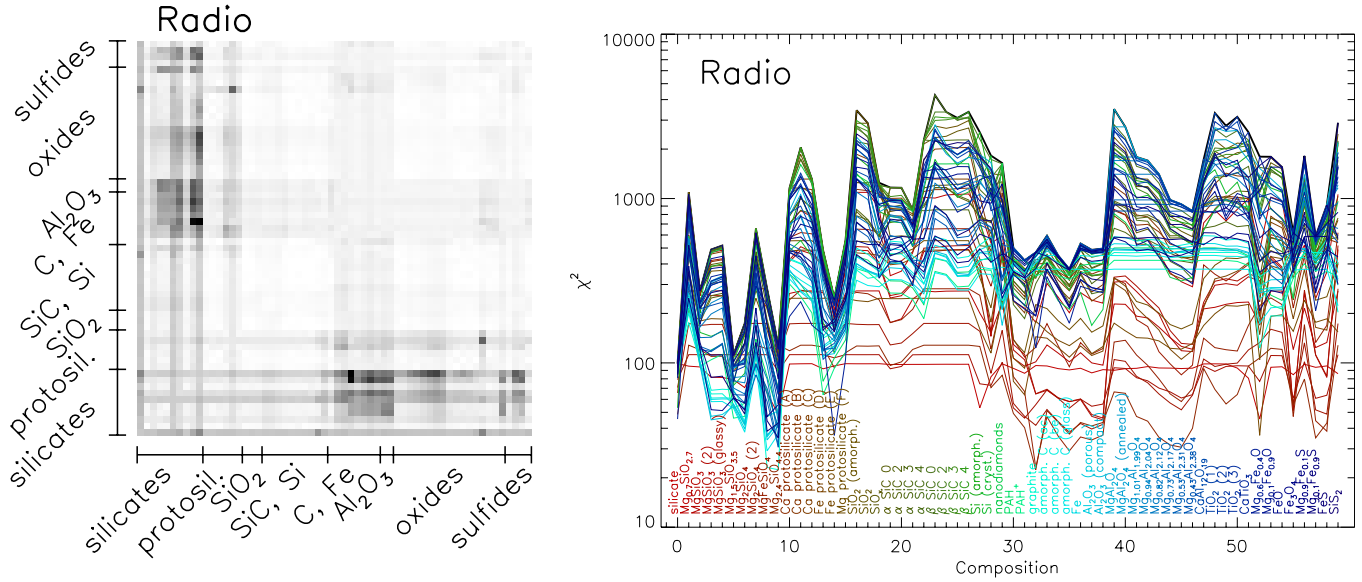

Figure 12. χ^2 as in Figure 7, but for the radio dust spectrum. The best fits here are for silicates with high Mg/Si ratios paired with the more featureless compositions.
(A color version of this figure is available in the online journal.)

Finally, Figure 16 also shows the best three-component model for the Ne II dust. The addition of TiO_2 nominally improves the fit over the best two-component model, but the changes to the spectrum are too minor to suggest that any third component is warranted.

4.4. X-Ray Fe Dust

The spectrum of dust associated with the X-ray Fe emission does exhibit apparent silicate peaks at ∼10 and 20 μm. The 10 μm peak is relatively weak, suggesting a lack of hot silicate grains. As with the Ar II dust, mixing silicate and more featureless emission (e.g., amorphous C) improves the quality of the fit. The preferred silicates here tend to have higher Mg/Si ratios than those that fit the Ar II and Ar III dust. Figure 17 shows the best two-composition fit. The temperatures for both components are warm, $T \approx 100$–112 K, with additional hot and cold components to account for the short and long wavelength emission. The figure also shows the best two-component fit that can be obtained without the use of silicate compositions. This marginal fit uses $Mg_{0.6}Fe_{0.4}O$ to adjust the shape of the model spectrum near 20 μm, but contains no replacement for a 10 μm silicate feature. The best three-component fit (see Figure 17) merely adds PAH^+ emission to reproduce a bump at 8 μm and sharpen the spectral feature at ∼10 μm. The overall change in χ^2 is small.

4.5. South Spot Dust

The South Spot spectrum looks rather different than the X-ray Fe spectrum, yet it tends to be best fit by similar dust compositions. Here the temperatures of the components that

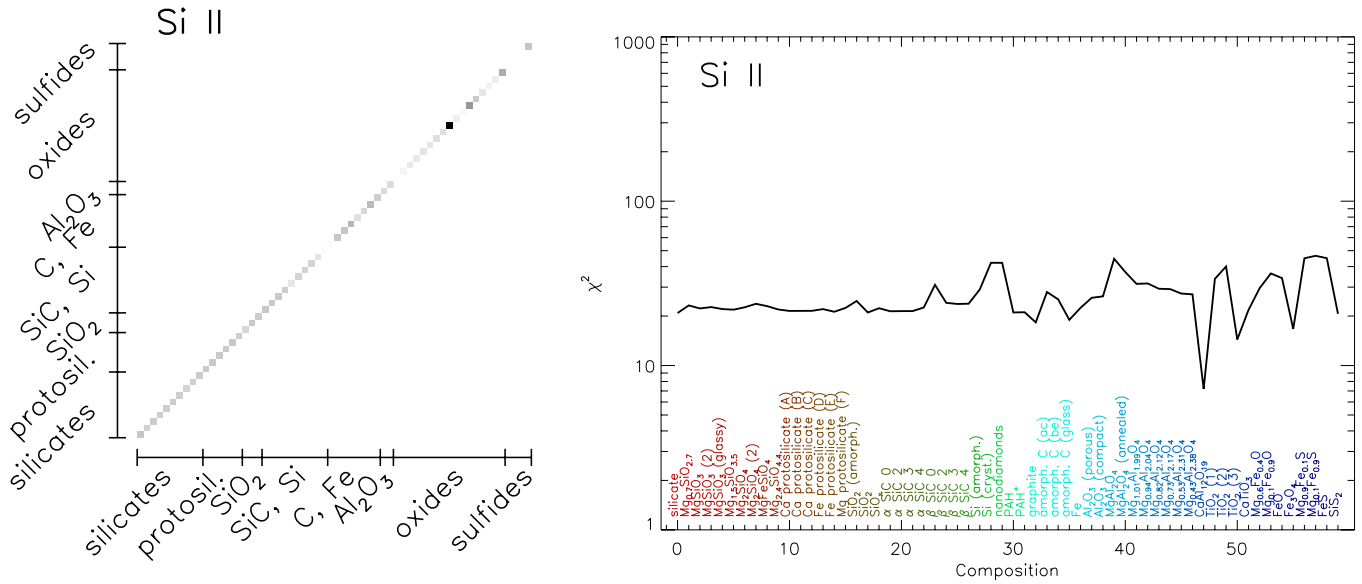

Figure 13. χ^2 as in Figure 7, but for the Si II dust spectrum. Only single-composition fits were performed because of the lack of detailed spectral constraints. The best fits are for compositions that have steeper long-wavelength absorption efficiencies, and for hibonite ($CaAl_{12}O_{19}$), which has a broad feature at $\sim$80 μm.
(A color version of this figure is available in the online journal.)

produce the <20 μm emission are higher than those for the X-ray Fe dust. Figure 18 shows the best two-component fit that uses similar compositions as the X-ray Fe spectrum (see, e.g., Figure 17). It also shows a marginal fit obtained without the use of silicates, and thus without any component that provides a 10 μm feature in the spectrum. The best three-component fit (see Figure 18) uses nonstoichiometric spinel to make minor adjustments to the shape of a good two-component model.

4.6. Radio (ISM) Dust

As for the X-ray Fe and South Spot spectra, the spectrum associated with the radio emission tends to be best fit with a mix of silicate and featureless dust (Figure 19). A marginal two-composition fit, in which $Mg_{0.1}Fe_{0.9}S$ serves as the "featureless" component across the 10–20 μm part of the spectrum is also shown in Figure 19. The best three-component fit (see Figure 19) is not significantly different from the best two-component fit, using two featureless components instead of one. The last example in Figure 19 shows the best results when dust compositions are restricted to the astronomical silicate, graphite, PAH, and PAH^+, which are commonly used to fit general interstellar material (e.g., Draine & Lee 1984; Zubko et al. 2004; Draine & Li 2007). The shape of the astronomical silicate's 10 μm emission peak is not as sharp as the observed spectrum. Cool PAH^+ emission provides sufficient adjustment to the shape of the silicate spectrum such that the model does not require graphite or neutral PAH components.

4.7. Si II Dust

The Si II dust spectrum essentially contains only the *Herschel* PACS measurements at 70, 100, and 160 μm, with only upper limits on the emission at shorter wavelengths. Because of this lack of detailed spectral information, the spectrum was only fit with single composition dust models. The measured Si II spectrum apparently has a relatively sharp peak compared to a blackbody spectrum. The best fit is provided by hibonite ($CaAl_{12}O_{19}$), which has a broad emission feature at $\sim$80 μm making it an especially good fit to the data. Figure 20 shows the best-fit spectrum ($CaAl_{12}O_{19}$), and a fit using a more typical Mg silicate (Mg_2SiO_4). Compositions that have a steeper spectral index at long wavelengths provide better fits, but the relatively good fit for TiO_2 (3) (rutile; second lowest χ^2 in Figure 13) is an artifact of an unphysically steep extrapolation ($\lambda^{-3.5}$) of the measured optical constants which are not published for $\lambda \geqslant$ 70 μm. For the Si II spectrum, any models that are within a factor of four of the minimum χ^2 are deemed acceptable. This includes most dust compositions and only excludes compositions that have strong features near $\sim$40 μm that would have exceeded the upper limits provided by the *Spitzer* IRS data.

5. DISCUSSION

5.1. Dust Compositions

The identifications of possible dust compositions in the different environments in Cas A are summarized in Table 4. A single dust composition can never provide a good fit to the observed spectra, except for the Si II spectrum which has only upper limits at <70 μm. In general, two compositions are sufficient to get acceptable fits to the spectra. The Ar II and Ar III spectra are the only ones that show significant (though small) benefit for the addition of a third composition. Among the seven characteristic dust spectra examined, the results can be grouped into three different families of dust.

The first family is found in association with the Ar II- and Ar III-emitting ejecta, which are distributed widely across the SNR. This family consists of the Mg silicate with the lowest Mg/Si ratio in combination with one or more other compositions that have featureless spectra. The $Mg_{0.7}SiO_{2.7}$ is a good fit to the 9 and 21 μm peaks in the observed spectrum, but only if a featureless dust composition is also present to reduce the apparent strength of these features. However, the Ar dust spectra also contain a weaker 12 μm feature which is not accounted for by any Mg silicate. Nonstoichiometric spinel with low Mg/Al ratios can provide a feature at approximately the correct wavelength, but only when the dust grains are extremely hot, such that longer wavelength spinel features are relatively faint. A better explanation for the 12 μm feature may be provided by

Table 4
Best Two-composition Fits of Cas A Dust

Spectrum	Compositions[a]	Total Dust Mass ($M_\odot$)[b]
Ar II	**$Mg_{0.7}SiO_{2.7}$** + [Graphite ‖ C (ac) ‖ FeS ‖ C (glass) ‖ Fe ‖ C (be) ‖ Al_2O_3 ‖ $Mg_xAl_yO_4$ ‖ Fe_3O_4]	0.01 ± 0.002
Ar III	**$Mg_{0.7}SiO_{2.7}$** + [$Mg_xAl_yO_4$ ‖ C (ac) ‖ Al_2O_3 ‖ C (glass) ‖ Fe ‖ C (be) ‖ Graphite ‖ $CaAl_{12}O_{19}$ ‖ Fe_3O_4]	0.004 ± 0.001
Ne II	**Al_2O_3** + [C (be) ‖ C (ac) ‖ C (glass) ‖ Fe ‖ Graphite ‖ FeS ‖ Fe_3O_4 ‖ $Mg_{0.1}Fe_{0.9}S$]	0.004 ± 0.001
X-ray Fe	**$Mg_{2.4}SiO_{4.4}$** + [C (be) ‖ C (glass) ‖ Fe ‖ $Mg_{0.1}Fe_{0.9}S$ ‖ C (ac) ‖ Graphite ‖ FeS ‖ Fe_3O_4] **$MgFeSiO_4$** + [C (be) ‖ C (glass) ‖ Fe ‖ $Mg_{0.1}Fe_{0.9}S$ ‖ C (ac)]	0.02 ± 0.01
South Spot	**$MgFeSiO_4$** + [C (glass) ‖ C (ac) ‖ C (be) ‖ Fe] **$Mg_{2.4}SiO_{4.4}$** + [C (ac) ‖ Fe ‖ C (be) ‖ C (glass)]	$0.0001 \pm 3 \times 10^{-5}$
Radio	**$Mg_{2.4}SiO_{4.4}$** + [Graphite ‖ $Mg_xAl_yO_4$ ‖ $Mg_{0.1}Fe_{0.9}S$ ‖ C (glass) ‖ PAH^+ ‖ Al_2O_3 ‖ FeS ‖ Fe ‖ C (be)] **$MgFeSiO_4$** + [Graphite ‖ C (glass) ‖ Al_2O_3 ‖ Fe ‖ C (be) ‖ FeS ‖ $Mg_{0.1}Fe_{0.9}S$]	0.0004 ± 0.0004
Si II	Indeterminate	$\lesssim 0.1$

Notes.
[a] The compositions in bold need to be paired with any one of the generally more featureless components listed after the "+" sign (i.e., ‖ indicates "or"). These components are listed in order of increasing χ^2, but the differences are not significant.
[b] Mean and σ for good models in which the bold components at left are the dominant mass.

Table 5
Possible Compositions for the 12 μm Peak of Ar II, Ar III Dust

Compositions	Comment
SiO_2	Requires CDE calculation of κ_λ, also contributes to 9 and 21 μm features
SiC	Requires CDE calculation of κ_λ
$Mg_xAl_yO_4$	Requires extremely high temperatures (>2000 K) [$y = (8–2x)/3$]
$CaAl_{12}O_{19}$	Requires extremely high temperatures (>2000 K)

SiO_2. The spectrum of SiO_2 exhibits all three peaks seen in Ar II and Ar III spectra, although they are significantly sharper and slightly bluer than the observed ones, and even in combination with other materials the fits are not very good. However, this is when Mie theory is used to calculate the absorption cross sections assuming small spherical grains. Using a CDE approximation instead broadens and shifts the SiO_2 features to be a better match as a third component. Jäger et al. (2003) point out that the 12 μm SiO_2 feature disappears in Mg silicates when Mg/Si > 0.5. Therefore, it seems likely that the dust associated with the Ar emission is a mixture of silica and Mg silicate (with Mg/Si $\lesssim$ 0.5) in combination with a separate featureless dust component. SiC can also provide the 12 μm feature, but again only if CDE calculations are applied to this component. If SiC is present, this would be the only direct evidence of carbon-bearing dust. Table 5 lists the possible origins for the 12 μm feature of the Ar dust.

The strong 21 μm peak in this family has been the hallmark of Cas A IR spectra since it was first observed using the Kuiper Airborne Observatory and the *Infrared Space Observatory (ISO)*. On the basis of those data, the peak was suggested to arise from Mg protosilicate (Arendt et al. 1999). Subsequent analysis by Douvion et al. (2001) modeled an *ISO* spectrum as $MgSiO_3$, SiO_2 and Al_2O_3 with the weak 12 μm feature largely produced by the Al_2O_3 as proposed for the feature in "spectrum 2" of Douvion et al. (1999). Ennis et al. (2006), using *Spitzer* IRS data, noted the distinction of several different dust spectra in different parts of Cas A and referred to this as the "strong 21 μm" spectrum. Calling it "21 μm peak dust," Rho et al. (2008) modeled it as Mg protosilicate and $MgSiO_3$ with secondary components of SiO_2, FeO, FeS, Si, and Al_2O_3 and/or Fe. Later work indicated that the 21 μm feature may be fit primarily by SiO_2 grains if CDE calculations rather than spherical grain approximations are used (Rho et al. 2009).

The second dust family is associated with the Ne II emission, which is especially prominent in two opposing "Ne crescents" (Ennis et al. 2006; Smith et al. 2009) in the north and south parts of the SNR. These morphological features are evident in the derived spatial distribution of the Ne II dust shown in Figure 4. This dust has a very smooth spectrum that does not suggest any silicate material. The best fits to the spectrum are found with Al_2O_3 in combination with other featureless dust. Featureless dust alone can provide moderately good fits, but a broad asymmetric feature in the 10–20 μm portion of the Al_2O_3 absorption cross section seems to match the observed spectrum especially well. Alternately, nonstoichiometric spinel can provide the needed emission at 10–20 μm, although the spinel absorption efficiency has more detailed substructure that is not evident in the observed spectrum.

This second family corresponds to the "weak 21 μm" components noted by (Ennis et al. 2006) and Rho et al. (2008), which they also associate with relatively strong Ne emission. However, the fact that they see even a weak 21 μm peak in their spectrum suggests that it is a mixture of what we identify as very distinct Ar and Ne dust families. As in our fitting, (Rho et al. 2008) fit this spectrum with hot and cool featureless dust (C glass) and with an intermediate temperature Al_2O_3 components. They included other components to add the weak 21 μm peak that appears in their spectrum. Douvion et al. (1999) had also noted an anti-correlation between the 9 μm silicate emission and Ne II and Ne III emission.

The third dust family is associated with the X-ray Fe emission and the South Spot. This family also seems to match the dust associated with the radio emission, which is expected to be dust that has been swept up from the ISM or CSM by the forward shock. The primary component in this family is one of the Mg silicates with high Mg/Si ratios or MgFe silicate: Mg_2SiO_4, $Mg_{2.4}SiO_{4.4}$, $MgFeSiO_4$. Other Mg silicates with Mg/Si $\geqslant$ 1 can provide acceptable fits, but the silicates with lower ratios that were needed for the Ar dust are not suitable here because of the changing placement and shape of the 9 and 21 μm features.

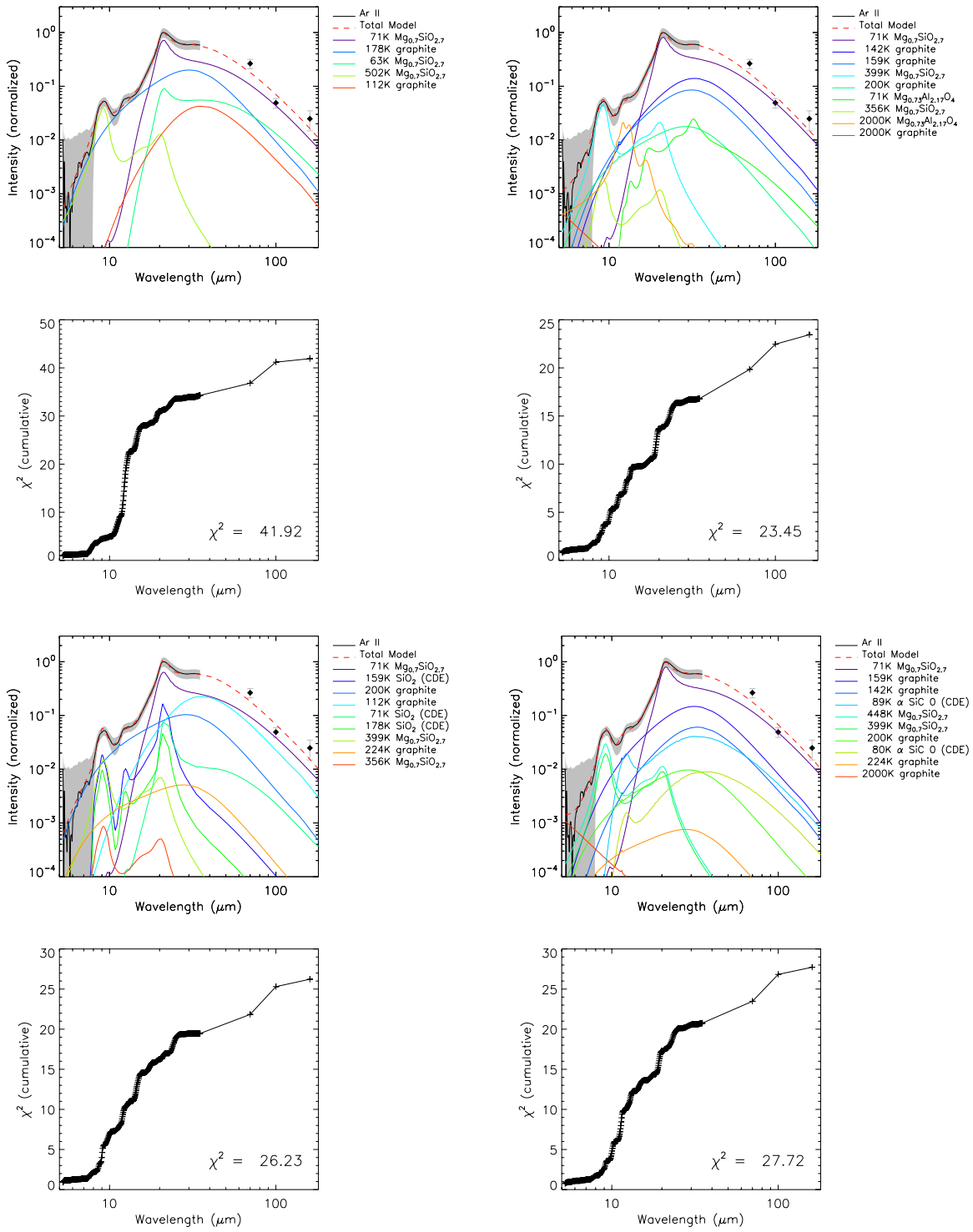

Figure 14. Upper left: the best two-composition fit to the Ar II spectrum includes $Mg_{0.7}SiO_{2.7}$ and a featureless dust composition. Uncertainties of the IRS data are indicated by the gray band. The lower panel shows how χ^2 accumulates as a function of wavelength. (upper right) The best three-component fit to the spectrum is a good match to all of the features at 9, 12 and 21 μm. However, the 12 μm feature is provided by implausibly hot nonstoichiometric spinel. (lower left) A very good three-component fit can also be obtained with SiO_2 as the third component, if its mass absorption coefficient is calculated via CDE rather than Mie theory. SiO_2 has features at each of the observed peaks. Lower right: another very good fit can be obtained with SiC as the third component, again if its mass absorption coefficient is calculated via CDE rather than Mie theory. SiC contributes only at 12 μm, but may also provide a partial match of the 21 μm feature (Jiang et al. 2005).

(A color version of this figure is available in the online journal.)

This dust family is matched by the "broad" component identified by Ennis et al. (2006) and the "featureless" component modeled by Rho et al. (2008). In both cases, this component is not associated with Ar or Ne emission lines, just as we also find. Rho et al. (2008) modeled this component as $MgSiO_3$, FeS, and Si combined with Al_2O_3, Mg_2SiO_4 and/or Fe. Using 5–17 μm *ISO* data, Douvion et al. (1999) extracted a spectrum ("Spectrum 3") from a region that should match our radio

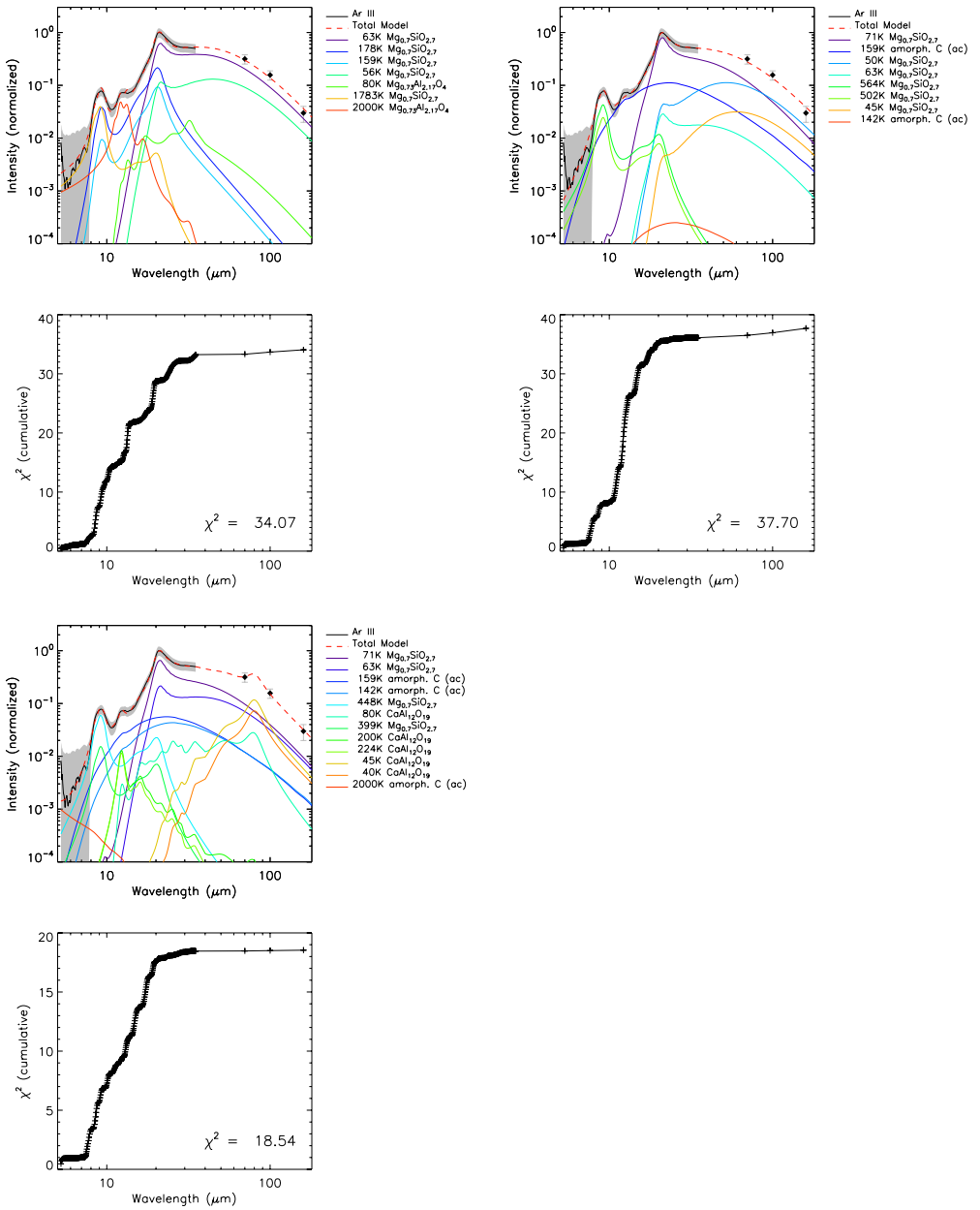

Figure 15. Upper left: best two-composition fit to the Ar III spectrum makes use of the 12 μm feature of nonstoichiometric spinel. Upper right: alternative two-component fits to the spectrum using featureless compositions (e.g., amorphous C) fit nearly as well, but do not match the 12 μm peak. Lower left: the best three-component fit uses $CaAl_{12}O_{19}$ (hibonite) to fit the 12 μm peak.

(A color version of this figure is available in the online journal.)

spectrum. Despite the limited wavelength coverage, they also found that the spectrum could be fit with astronomical silicate (Draine & Lee 1984) at $T \sim 105$ K, as we confirm (in Figure 19).

The Si II dust has no significant emission across the 5–40 μm wavelength range of the IRS. The three *Herschel* PACS measurements at 70, 100, and 160 are insufficient to constrain the composition of the associated dust. The Si II dust may belong to one of the above families or it may be an entirely different composition.

5.2. Dust Masses

The modeled dust temperatures and compositions allow for the determination of the dust mass in each of the components. The dust mass, M_d, is calculated as

$$M_d = \frac{D^2 S_\nu(\lambda)}{\kappa_\nu(\lambda) B_\nu(\lambda, T_d)}, \quad (4)$$

where $D = 3.4$ kpc is the distance to Cas A (Reed et al. 1995), $S_\nu(\lambda)$ is the total flux density of the component in question, $\kappa_\nu(\lambda)$ is the mass absorption coefficient appropriate for the derived composition of the dust, and $B_\nu(\lambda, T_d)$ is the Planck function evaluated at the derived temperature. For each of the models fit to the characteristic spectra, the total mass was calculated by summing Equation (4) over all temperature components of each of the compositions used in the fit. Generally, the total dust mass is dominated by a warm component (60–130 K) that also produces the bulk of the luminosity. However, the

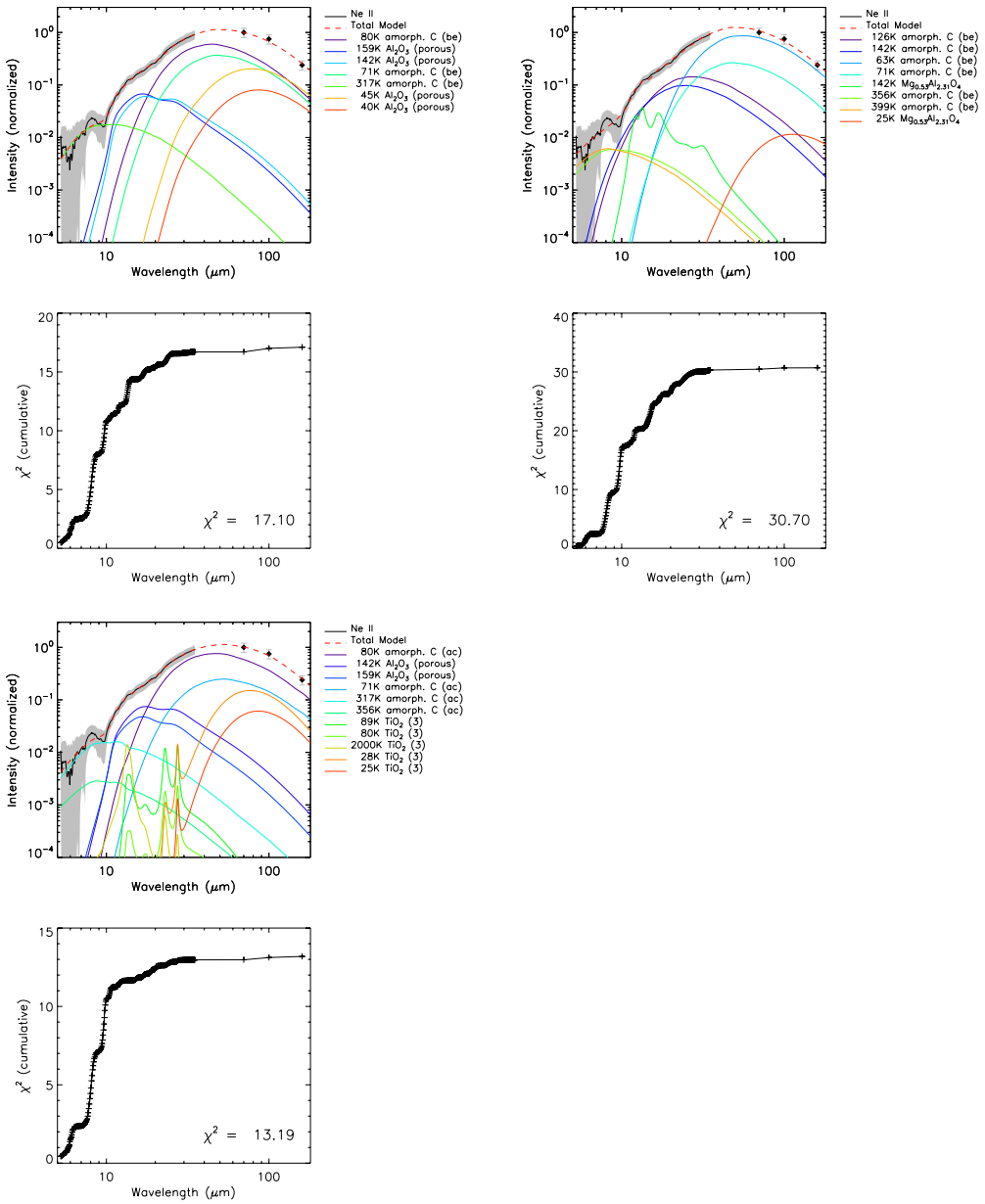

Figure 16. Upper left: best two-component fits to the Ne II spectrum use Al_2O_3 in combination with a more featureless component. None of the silicates are a good match for this very smooth spectrum. Upper right: an alternative two-component fit to the spectrum can be found using nonstoichiometric spinel instead of Al_2O_3. Lower left: the best three-component fit adds TiO_2, but the improvement in the fit is very small and does not justify the addition of the third composition.

(A color version of this figure is available in the online journal.)

X-ray Fe spectrum is an exception where an additional cold component dominates the mass because the *Herschel* PACS data at 70–160 μm are elevated relative to the shorter wavelength emission. The composition of this cold component is uncertain because absorption efficiencies are smooth and the spectral resolution is poor at the long wavelengths. This situation is worse for the Si II dust which is only detected at $\geqslant$70 μm. Its temperature is relatively well constrained, but its composition, and therefore its mass, is not. If the dust is composed of Mg silicates, then the total mass of the Si II dust is $\lesssim$0.1 $M_\odot$, but this value can be much lower if other compositions are appropriate. Much higher masses are ruled out by the expected nucleosynthetic yields of various elements, and would imply very high condensation efficiencies given that the mass of the unshocked gas is only $\sim$0.4 $M_\odot$ (DeLaney et al. 2014).

The derived dust masses averaged over all models that fit within a factor of two of the minimum χ^2 and are dominated by Mg silicates (or Al_2O_3 for the Ne II spectrum) are listed in Table 4. Figure 21 plots the total dust mass for *all* two-component models of the Ar II dust spectrum as a function of χ^2 with color coding to indicate compositions and temperatures. The "good" models are within a factor of two of the minimum χ^2 (to the left of the dashed line). The figure shows that although there are correlations between composition and temperatures, the derived mass is more strongly dependent on the composition than the temperature.

The total mass of warm and hot dust for all components that contribute to the <35 μm spectrum is found to be $0.04 \pm 0.01\ M_\odot$ (see Table 3). This is consistent with other measurements from *IRAS* (Braun 1987; Arendt 1989;

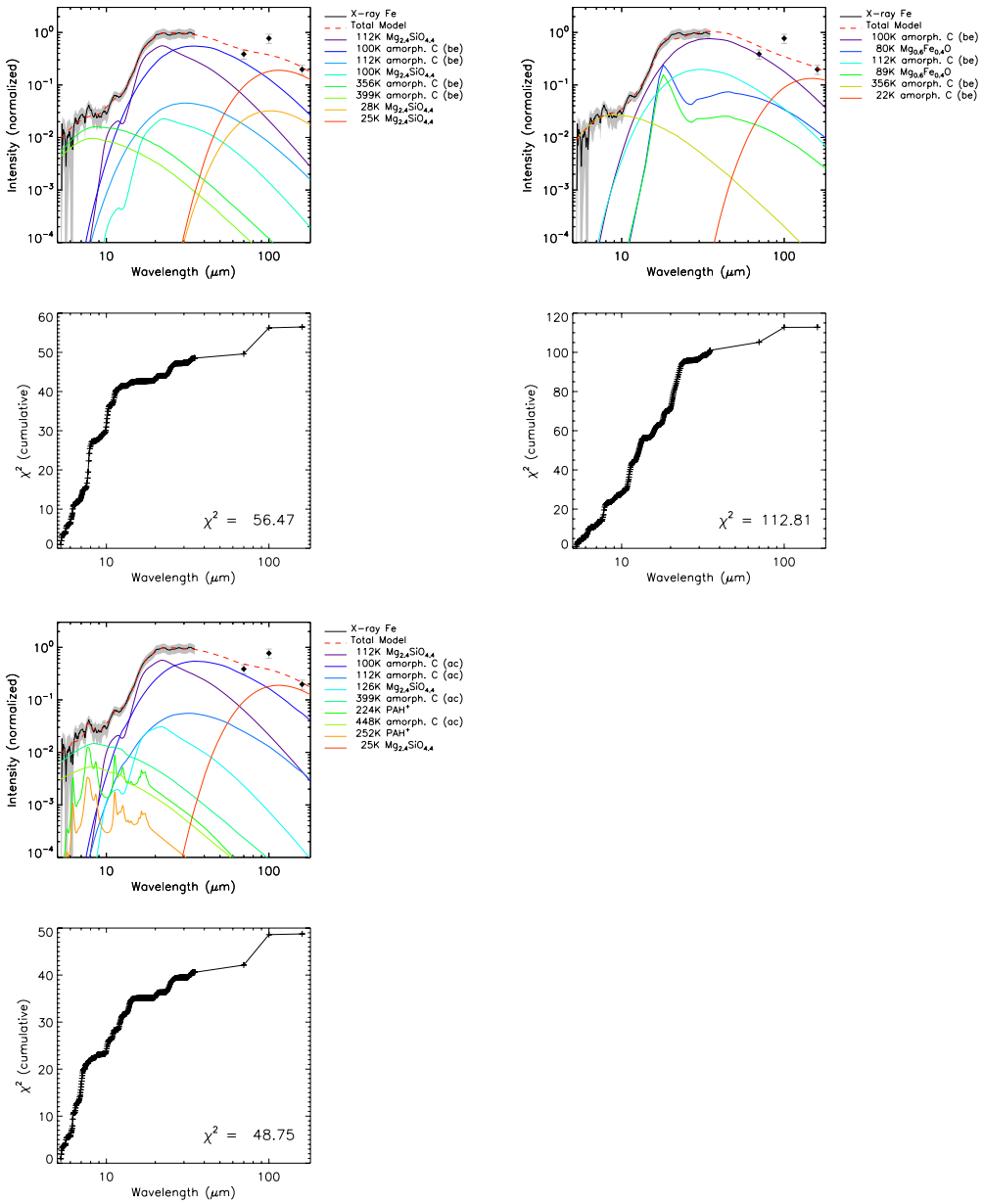

Figure 17. Upper left: best two-component fit to the X-ray Fe spectrum uses a Mg silicate in combination with a featureless composition. Upper right: this alternative two-component fit (without silicates) is about a factor of two worse than the best fit, and is thus only marginally acceptable. Lower left: the best three-component fit uses ionized PAHs to match the small (and possibly spurious) bump at 8 μm.

(A color version of this figure is available in the online journal.)

Saken et al. 1992) and other analysis of the *Spitzer* IRS data (Rho et al. 2008) because the mid-IR (12–100 μm) flux density $S_\nu(\lambda)$ remains basically the unchanged since the *IRAS* measurements. This is the primary observable factor in determining the mass. When corrected for the same distance, previously published mass estimates contain modest differences (factors of ~two) due to different assumptions of the mass absorption coefficients, $\kappa_\nu(\lambda)$, and dust temperature, T_d. *ISO*, *Akari*, BLAST, and *Herschel* have revealed an additional cool dust component in Cas A which contains ~0.08 $M_\odot$ of dust (e.g., Tuffs et al. 1999, 2005; Sibthorpe et al. 2010; Barlow et al. 2010). This cool component is what we associated with the Si II. Our mass estimate of this component is consistent, but is very uncertain due to the unknown composition of the dust, and the difficulty in distinguishing the SNR dust from the heavy confusion of the line of sight ISM at these wavelengths.

6. SUMMARY

We have decomposed the spatially resolved IR continuum spectra of dust in the Cas A SNR into contributions from distinct regions of the remnant, comprising shocked CSM and ISM swept up by the forward shock, hot X-ray-emitting gas and cooler, denser fine-structure IR line-emitting regions that result when the SN ejecta passes through the reverse shock, and unshocked regions of the ejecta that have not yet reached the reverse shock. We then calculated the composition and mass of the dust associated with each region of the ejecta. The methodology and results of our paper can be summarized as follows.

1. We started by identifying a set of *spatial templates* to represent various IR-emitting regions of Cas A. These were defined by the fine structure IR lines from Ar II, Ar III,

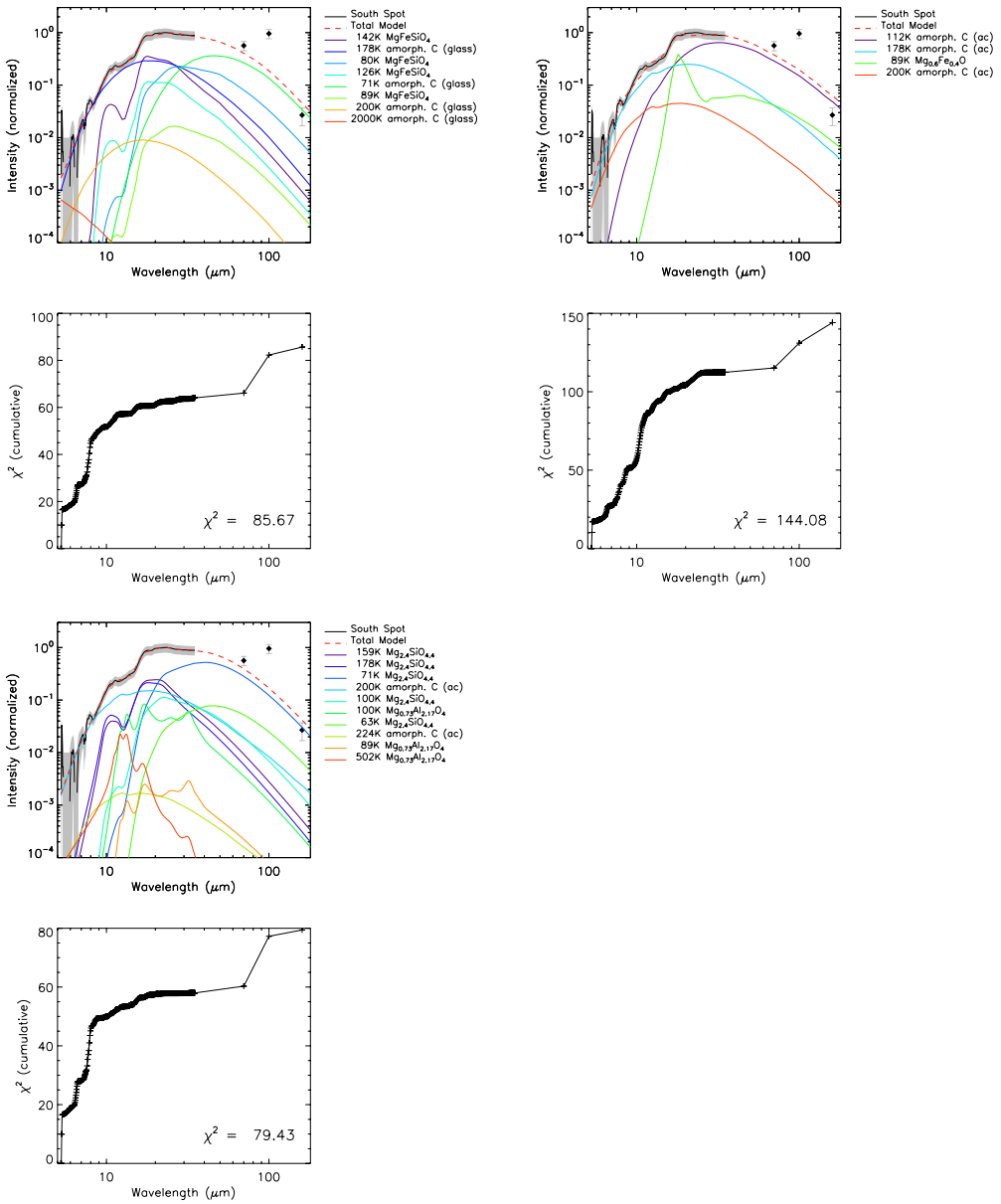

Figure 18. Upper left: best two-component fits to the South Spot spectrum are similar to those for the X-ray Fe spectrum, but involved higher dust temperatures for the dominant components. Upper right: an alternative two-component fit again shows that reasonable (though worse) fits can also be obtained without the use of silicates. Lower left: the best three-component fit uses nonstoichiometric spinel as a third component to make relatively minor adjustments to the model.

(A color version of this figure is available in the online journal.)

Ne II, and Si II; by the X-ray (Fe line); and by the radio synchrotron emission. The spatial templates used for the decomposition are shown in Figure 1.

2. We then identified spatially distinct *zones*, shown in Figure 2, in which a given template emission was dominant. We extracted the *characteristic spectra* of the dust in each zone using the procedure described in Section 3. The resulting IR spectra were assumed to represent the different spatial templates, and are presented in Figure 3. Figure 4 shows the derived *spatial distribution* of the dust associated with each of the spectral templates.
3. We compiled an extensive list of dust compositions with measured optical constants to calculate their possible contribution to the IR emission from each spatial templates. The dust species fall into eight broad categories defined by similarity of chemical and/or optical properties: silicates, protosilicates, silica, silicon carbide, carbon and metallic iron, aluminum oxides, oxides, and sulfides. The dust compositions used in the analysis are listed in Table 2.
4. We fit each characteristic spectrum with all possible combinations of two distinct dust species (1711 combinations), allowing each dust species to emit at a range of temperatures. Figures 7–13 depict the χ^2 values to give an overview of which compositions can provide good fits to the characteristic spectra. Figures 14–20 provide examples of how well the spectra can be fit using two (and sometimes three) dust species.
5. The primary dust composition could be readily identified in spectra that have strong IR dust features. The Ar II and Ar III characteristic spectra exhibited strong features at ~9 and 21 μm. Magnesium silicates, characterized by a Mg/Si ratio of 0.7 (i.e., $Mg_{0.7}SiO_{2.7}$) provided the best fit

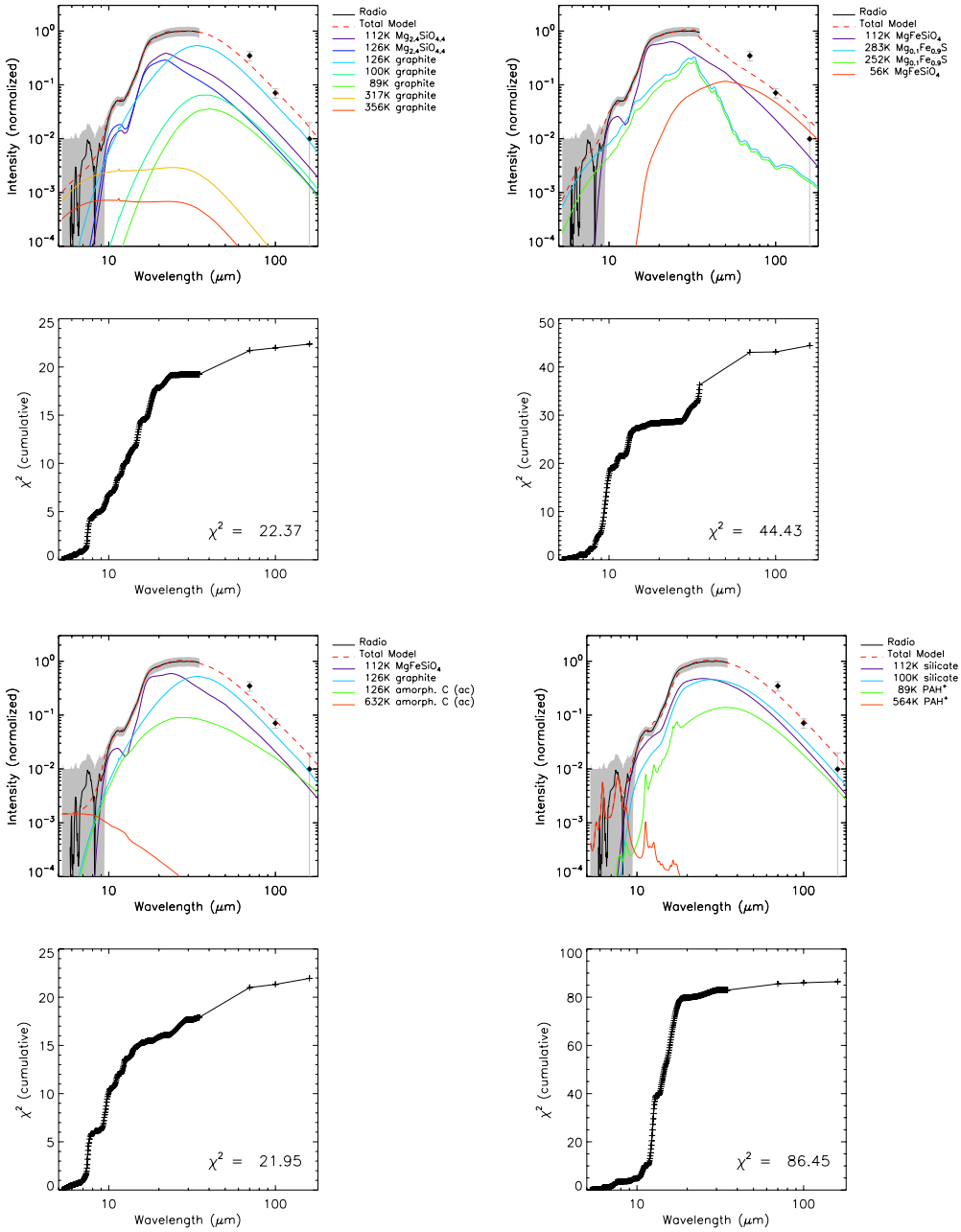

Figure 19. Upper left: best two-component fit to the Radio spectrum uses graphite and a Mg silicate. Combinations of other silicates with other featureless components are nearly as good. Upper right: this alternate fit to the Radio spectrum shows a marginal model using a sulfide composition instead of a one of the more featureless dust compositions. Lower left: the best three-component fit is only very slightly better than the two-component fit. Lower right: the fit using the standard astronomical silicate, graphite, PAH, and PAH$^+$ combination. Only two of the four components are actually needed for the fit since the PAH$^+$ component is sufficient to provide a relatively featureless component at $\gtrsim$20 μm and the PAH emission band at $\sim$8 μm.

(A color version of this figure is available in the online journal.)

to the spectra of these regions. The Ne II spectrum was best fit with Al_2O_3 dust, and the X-ray Fe spectrum, which exhibit peaks at $\sim$10 and 20 μm was best fit with silicates having a higher Mg/Si ratio of 2.4 (i.e., $Mg_{2.4}SiO_{4.4}$). A region called the South Spot had similar composition. The dust composition associated with the spectrum of the radio synchrotron-emitting region behind the SNRs forward shock was consistent with that expected for typical interstellar dust. The IR spectrum from the Si II-emitting region arises from a cold dust component that is only seen at long wavelengths. Since very few dust compositions have distinguishing features at these wavelengths, and because these broad band data at long wavelengths provide little detail on the spectrum, the composition of this cold dust could not be determined.

6. Secondary dust components are needed to improve the fit for most spectra, but these components are not uniquely identified. Table 3 lists the primary dust composition for each spectrum, and all possible secondary dust species that they need to be paired with. The secondary dust species generally have a featureless dust spectrum.
7. A minimal number of only four dust species, $Mg_{0.7}SiO_{2.7}$, $Mg_{2.4}SiO_{4.4}$, Al_2O_3, and amorphous carbon, would be sufficient to fit the entire spectrum of Cas A.

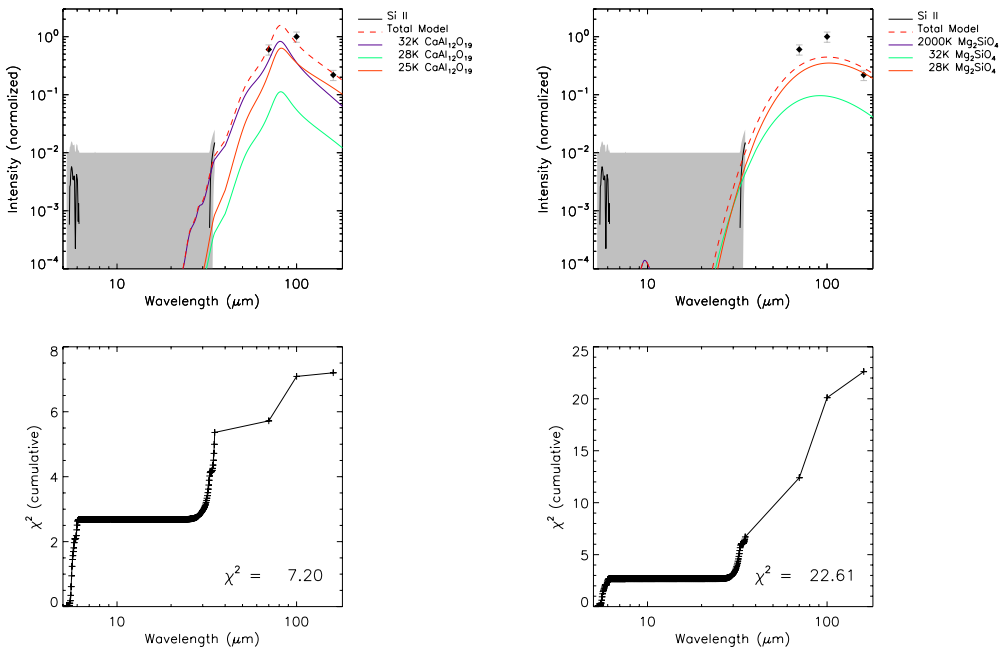

Figure 20. Left: best one-component fit to the Si II spectrum uses $CaAl_{12}O_{19}$, which happens to have a broad peak in its absorption efficiency at ~80 μm Right: this alternative fit uses Mg_2SiO_4 which has a more typical power law absorption efficiency with an index of −2 at long wavelengths.

(A color version of this figure is available in the online journal.)

These compositions suggest that the seed dust particles that formed the more complex species are MgO, SiO_2, Al_2O_3, and carbon.

8. The total mass of dust is about 0.04 $M_\odot$ in the shocked CSM/ISM and ejecta regions, and $\lesssim$0.1 $M_\odot$ in the unshocked ejecta characterized by the Si II emission. This dust mass is similar to that derived by Rho et al. (2008) from the *Spitzer* data, and the ~0.08 $M_\odot$ derived for dust in the cold unshocked ejecta derived from the *Herschel*, BLAST, and *Akari* data (Barlow et al. 2010; Sibthorpe et al. 2010).

This work is based on observations made with the *Spitzer Space Telescope*, which is operated by the Jet Propulsion Laboratory, California Institute of Technology, under a contract with NASA. Support for this work was provided by NASA Program NNH09ZDA001N-ADP-0032. This research made use of Tiny Tim/*Spitzer*, developed by John Krist for the Spitzer Science Center. The Center is managed by the California Institute of Technology under a contract with NASA. This research has made use of NASA's Astrophysics Data System Bibliographic Services. We thank T. Kozasa for providing digitized (and extrapolated and interpolated) versions of the optical constants for several dust species as noted in Table 3. We also thank the referee for constructive comments on the manuscript.

Facilities: Spitzer, *Herschel*, *CXO*, VLA

APPENDIX

SELECTION OF SPATIAL TEMPLATES

A set of spatial templates are needed to distinguish different physical environments within the SNR. We aim to be able to distinguish swept up ISM or CSM dust from ejecta dust, to probe the nature of ejecta dust created in different nucleosynthetic layers of the SN, and to investigate ejecta dust in preshock and postshock regions having different gas temperatures and densities. The primary source for templates are the line emission maps that are generated by subtracting the continuum cube from the full data cube, and then integrating over the [−6000, +8000] km s^{-1} velocity range for each of the emission lines in the IRS spectrum (see Table 1). Most of these lines are associated with the FMKs of ejecta. These knots tend to be O-rich, but there are some variations in composition that tend to be correlated with spatial and kinematic differences. Because of the large range in velocity in the Cas A ejecta, closely spaced [O IV] 25.89 μm and [Fe II] 25.99 μm lines would be confused in the low-resolution spectra. However, Isensee et al. (2010, 2012) report that high-resolution spectra show that Cas A's 26 μm line is entirely produced by [O IV] without any contribution from [Fe II].

Several other spatial templates were also tested. These are intended to trace the presence of dust in a wider range of environments than the relatively cool and dense line-emitting knots.

1. A radio template was derived from 6 cm VLA image of Cas A (DeLaney 2004). The region of the forward shock is traced more clearly in the radio than at most other wavelengths, and the bright radio knots in the reverse shock region are a different population than line-emitting ejecta knots.
2. and 3. X-ray Fe and Si templates were derived from *Chandra* observations (Hwang et al. 2004), integrated over the widths of the 6.4 keV Fe and 1.7 keV Si K α lines. The X-ray continuum is included in these integrations. These templates trace ejecta in regions of lower density and much higher temperature. These regions include the bulk of the mass of the ejecta of the SN.
4. The IRAC 4.5 μm image lies outside the range of the IRS spectral coverage and contains both a synchrotron component and a probable line emission component. The synchrotron emission was subtracted using a scaled version of the IRAC 3.6 μm image which is dominated by synchrotron

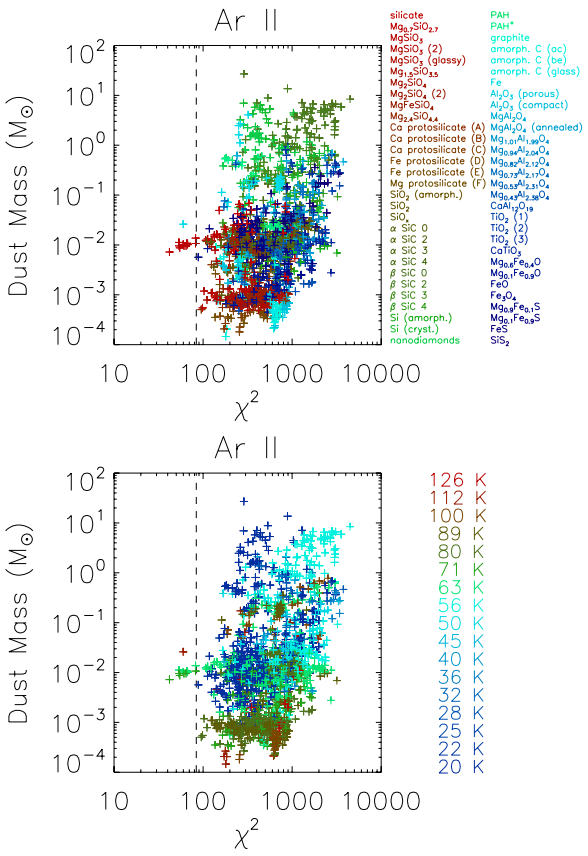

Figure 21. Total dust masses for Ar II models. In the top panel, the points are color coded by the composition that provides the largest mass component. In the bottom panel, the masses are color coded by the temperature of the dominant mass component. Only models to the left of the dashed line (within a factor of two in χ^2 of the best model) are deemed acceptable. These good models indicate that $\sim 10^{-2}\ M_{\odot}$ of dust, mostly silicates at ~70 K, is associated with the Ar II emission in Cas A.

(A color version of this figure is available in the online journal.)

emission and has only weak line emission. However, this over-subtracts stellar sources in the image. Thus, regions where negative values resulted were replaced by nearby background values.

5. The IRAC 8 μm image is dominated by the [Ar II] 6.99 μm emission, but was considered as a potentially cleaner map of this line than the IRS line maps. The background ISM emission at 8 μm was removed by subtracting a scaled version of the 5.8 μm IRAC image, where the SNR emission is relatively weaker. As with the 4.5 μm template, the over-subtracted stellar sources were replaced by the local background levels.

Each of these templates is convolved and reprojected to match the IRS continuum data cube.

This full set of templates would be expected to contain some degeneracies, where different lines (especially from the same species or element) would be tracing the same physical component of the SNR. To select a useful subset of the possible templates, we calculated the linear correlation coefficient for each pair of templates. These are listed in Table 1. The table shows which templates are well-correlated with others. Based on these correlations we sorted the templates in to similar groups and selected one template to represent each group. Images of the selected templates are shown in Figure 1.

There are several points of interest in the correlations listed in Table 1. Even though the [Ar II] and [Ar III] emission are very well correlated (as expected), we chose to keep both these templates in order to monitor for changes in the dust that might be related to the ionization state of the gas. It was not expected that highly ionized species such as [S IV] would correlate so well with [Ar II]. This correlation may become significantly weaker if higher spatial resolution data were available. Correlations involving the [Fe II] line are weaker than most due to the low signal to noise ratio of this line. The [Ne V] line is also relatively weak, yet surprisingly it correlates better with the [Ar II] group than the [Ne II] and [Ne III] lines. Despite an absence of Ne lines in the band, the 4.5 μm IRAC μm emission is somewhat better correlated with the Ne group templates than the Ar group. In particular, the "Ne crescents" noted by Ennis et al. (2006) are present in the IRAC 4.5 μm image. Although the [S III] 33.48 μm correlates moderately well with the [S III] 18.71 μm line, it does not correlate as well with the other templates of the Ar group. This is an indication of variation in the S III line ratios, which would indicate large scale variations in the density of the ejecta (Smith et al. 2009). The [O IV] 25.89 μm and [S III] 33.48 μm templates are moderately correlated with the both the Si II template and the Ar-like templates. Because the [O IV] and [S III] templates did not have distinct features lacking in these other templates, we did not use either in the analysis. The X-ray Si template is in fact distinct from the X-ray Fe template, but it was not used because initial analysis using only the X-ray Fe template did not indicate the presence of any residual emission that would have been reduced by the addition of an X-ray Si template.

REFERENCES

Arendt, R. G. 1989, ApJS, 70, 181
Arendt, R. G., Dwek, E., & Moseley, S. H. 1999, ApJ, 521, 234
Barlow, M. J., Krause, O., Swinyard, B. M., et al. 2010, A&A, 518, L138
Begemann, B., Dorschner, J., Henning, T., & Mutschke, H. 1996, ApJL, 464, L195
Begemann, B., Dorschner, J., Henning, T., Mutschke, H., & Thamm, E. 1994, ApJL, 423, L71
Begemann, B., Dorschner, J., Henning, T., et al. 1997, ApJ, 476, 199
Biscaro, C., & Cherchneff, I. 2014, A&A, 564, 25
Bohren, C. F., & Huffman, D. R. 1983, Absorption and Scattering of Light by Small Particles (New York: Wiley)
Braatz, A., Ott, U., Henning, T., Jäger, C., & Jeschke, G. 2000, M&PS, 35, 75
Brandt, T. D., & Draine, B. T. 2012, ApJ, 744, 129
Braun, R. 1987, A&A, 171, 233
Cherchneff, I. 2012, A&A, 545, A12
Cherchneff, I., & Dwek, E. 2010, ApJ, 713, 1
Clayton, D. D. 2013, ApJ, 762, 5
DeLaney, T., Kassim, N. E., Rudnick, L., & Perley, R. A. 2014, ApJ, 785, 7
DeLaney, T. A. 2004, PhD thesis, Univ. Minnesota
Dorschner, J., Begemann, B., Henning, T., Jaeger, C., & Mutschke, H. 1995, A&A, 300, 503
Dorschner, J., Friedemann, C., Guertler, J., & Duley, W. W. 1980, Ap&SS, 68, 159
Douvion, T., Lagage, P. O., & Cesarsky, C. J. 1999, A&A, 352, L111
Douvion, T., Lagage, P. O., & Pantin, E. 2001, A&A, 369, 589
Draine, B. T., & Lee, H. M. 1984, ApJ, 285, 89
Draine, B. T., & Li, A. 2007, ApJ, 657, 810
Dwek, E., & Cherchneff, I. 2011, ApJ, 727, 63
Edoh, O. 1983, PhD thesis, The Univ. Arizona
Edwards, D. F. 1985, in Handbook of Optical Constants of Solids, ed. E. D. Palik (San Diego, CA: Acedemic), 547
Ennis, J. A., Rudnick, L., Reach, W. T., et al. 2006, ApJ, 652, 376
Fabian, D., Henning, T., Jäger, C., et al. 2001, A&A, 378, 228
Fesen, R. A., Hammell, M. C., Morse, J., et al. 2006, ApJ, 645, 283
Forrest, W. J., Houck, J. R., & McCarthy, J. F. 1981, ApJ, 248, 195
Gordon, K. D., Engelbracht, C. W., Rieke, G. H., et al. 2008, ApJ, 682, 336
Griffin, M. J., Abergel, A., Abreu, A., et al. 2010, A&A, 518, L3
Henning, T., Begemann, B., Mutschke, H., & Dorschner, J. 1995, A&AS, 112, 143

Hony, S., Waters, L. B. F. M., & Tielens, A. G. G. M. 2002, A&A, 390, 533
Hwang, U., Laming, J. M., Badenes, C., et al. 2004, ApJL, 615, L117
Isensee, K., Olmschenk, G., Rudnick, L., et al. 2012, ApJ, 757, 126
Isensee, K., Rudnick, L., DeLaney, T., et al. 2010, ApJ, 725, 2059
Jaeger, C., Mutschke, H., Begemann, B., Dorschner, J., & Henning, T. 1994, A&A, 292, 641
Jäger, C., Dorschner, J., Mutschke, H., Posch, T., & Henning, T. 2003, A&A, 408, 193
Jiang, B. W., Zhang, K., & Li, A. 2005, ApJL, 630, L77
Krause, O., Birkmann, S. M., Usuda, T., et al. 2008, Sci, 320, 1195
Li, A., & Draine, B. T. 2001, ApJ, 554, 778
Lynch, D. W., & Hunter, W. R. 1991, in Handbook of Optical Constants of Solids II, ed. E. D. Palik (San Diego, CA: Acedemic), 341
Markwardt, C. B. 2009, in ASP Conf. Ser. 411, Astronomical Data Analysis Software and Systems XVIII, ed. D. A. Bohlender, D. Durand, & P. Dowler (San Francisco, CA: ASP), 251
Mukai, T. 1989, in Evolution of Interstellar Dust and Related Topics, ed. A. Bonetti, J. M. Greenberg, & S. Aiello (Amsterdam: Elsevier), 397
Mutschke, H., Andersen, A. C., Jäger, C., Henning, T., & Braatz, A. 2004, A&A, 423, 983
Mutschke, H., Posch, T., Fabian, D., & Dorschner, J. 2002, A&A, 392, 1047
Nozawa, T., Kozasa, T., Tominaga, N., et al. 2010, ApJ, 713, 356
Nozawa, T., Kozasa, T., Tominaga, N., et al. 2008, ApJ, 684, 1343
Omont, A., Moseley, S. H., Cox, P., et al. 1995, ApJ, 454, 819
Philipp, H. R. 1985, in Handbook of Optical Constants of Solids, ed. E. D. Palik (San Diego, CA: Acedemic), 749
Pilbratt, G. L., Riedinger, J. R., Passvogel, T., et al. 2010, A&A, 518, L1
Piller, H. 1985, in Handbook of Optical Constants of Solids, ed. E. D. Palik (San Diego, CA: Acedemic), 571
Poglitsch, A., Waelkens, C., Geis, N., et al. 2010, A&A, 518, L2
Posch, T., Kerschbaum, F., Fabian, D., et al. 2003, ApJS, 149, 437
Reed, J. E., Hester, J. J., Fabian, A. C., & Winkler, P. F. 1995, ApJ, 440, 706
Rest, A., Foley, R. J., Sinnott, B., et al. 2011, ApJ, 732, 3
Rho, J., Kozasa, T., Reach, W. T., et al. 2008, ApJ, 673, 271
Rho, J., Reach, W. T., Tappe, A., et al. 2009, in ASP Conf. Ser. 414, Cosmic Dust—Near and Far, ed. T. Henning, E. Grün, & J. Steinacker (San Francisco, CA: ASP), 22
Rinehart, S. A., Benford, D. J., Cataldo, G., et al. 2011, ApOpt, 50, 4115
Rouleau, F., & Martin, P. G. 1991, ApJ, 377, 526
Saken, J. M., Fesen, R. A., & Shull, J. M. 1992, ApJS, 81, 715
Semenov, D., Henning, T., Helling, C., Ilgner, M., & Sedlmayr, E. 2003, A&A, 410, 611
Sibthorpe, B., Ade, P. A. R., Bock, J. J., et al. 2010, ApJ, 719, 1553
Siebenmorgen, R., Voshchinnikov, N. V., & Bagnulo, S. 2014, A&A, 561, A82
Smith, J. D. T., Rudnick, L., Delaney, T., et al. 2009, ApJ, 693, 713
Tuffs, R. J., Fischera, J., Drury, L. O., et al. 1999, in ESA Special Publication, Vol. 427, The Universe as Seen by ISO, ed. P. Cox & M. Kessler (Noordwijk: ESA), 241
Tuffs, R. J., Popescu, C. C., & Völk, H. J. 2005, in ESA Special Publication, Vol. 577, ed. A. Wilson (Noordwijk: ESA), 427
Valiante, R., Schneider, R., Salvadori, S., & Bianchi, S. 2011, MNRAS, 416, 1916
Zeidler, S., Posch, T., Mutschke, H., Richter, H., & Wehrhan, O. 2011, A&A, 526, A68
Zinner, E. 2008, PASA, 25, 7
Zubko, V., Dwek, E., & Arendt, R. G. 2004, ApJS, 152, 211